

# Effects of build orientation and strain rate on the tensile-shear behaviour of polyamide-12 manufactured via laser powder bed fusion

Yuan Xu<sup>a,b,\*</sup>, Gustavo Quino<sup>a,c,d</sup>, Karthik Ram Ramakrishnan<sup>c</sup>, Antonio Pellegrino<sup>a,\*</sup>

<sup>a</sup> Department of Engineering Science, University of Oxford, OX1 3PJ, UK

<sup>b</sup> School of Engineering, Newcastle University, Newcastle upon Tyne, NE1 7RU, UK

<sup>c</sup> Bristol Composites Institute, University of Bristol, BS8 1TL, UK

<sup>d</sup> Department of Aeronautics, Imperial College London, SW7 2AZ, UK

## ARTICLE INFO

### Keywords:

Powder bed fusion  
Polyamide-12 (PA12)  
Tension-torsion  
Scanning electron microscopy  
Hopkinson bar  
Rate dependence

## ABSTRACT

Laser powder bed fusion (L-PBF) of engineering thermoplastics is a well-established additive manufacturing technique. In this work, an experimental investigation of the tensile-shear behaviour of L-PBF processed polyamide-12 (PA12) is presented, with a particular focus on the concurrent effect of build orientation and rate dependency at strain rates ranging from  $10^{-3}$  to  $10^3 \text{ s}^{-1}$ . Results show that the deformation behaviour features significant anisotropy at both low and high strain rates, while quasi-static ultimate strength in either tension or shear shows no dependence on the build direction. As the strain rate increases, the tensile strength is characterised by apparent positive rate dependence but remains insensitive to the build orientation; however the shear strength displays significant build orientation-dependent anisotropy, highlighted by the decreasing shear strength of specimens printed in the loading direction. Post-mortem scanning electron microscopy (SEM) demonstrates torn dimples with stretched filaments in quasi-static fractography, while cleavage facets with flake structures retrieved from high-rate loading. A fibrillar structure is observed from high-rate torsional loading indicating adiabatic decohesion during rapid crack propagation. These findings draw attention to the significant anisotropy of L-PBF PA12 parts in a high-rate loading regime and provide directions to improve the current L-PBF techniques.

## 1. Introduction

Additive Manufacturing (AM), popularly dubbed 3D printing, is a transformative manufacturing technique in which complex three-dimensional parts are built by joining materials layer by layer. AM parts are increasingly used in industrial applications ranging from biomedical to aerospace and automotive engineering [1,2]. Powder bed fusion (PBF) is a type of AM process in which a bed of powder is selectively heated by a high-power directional laser (for L-PBF process) or electron beam (for E-PBF process) to form a solidified layer of fused powder and the process is repeated layer by layer [3]. PBF process offers many advantages such as faster design to manufacturing cycle, high printing resolution, ability to print complex geometries without additional support, and inexpensive production of small numbers of parts [4]. The common materials used in AM are engineering thermoplastics such as polyamides (PA), polyimides (PI), polyetherimides (PEI), and polycarbonates (PC). Currently, polyamide-12 (PA12) is the most widely

used powder material that accounts for over 90% of polymeric PBF workpieces owing to the combination of easy processability, low cost, lightweight, and impact resistance [5,6].

Due to the numerous merits, the use of AM technology has shifted progressively from prototyping towards the production of end-use parts [6–8]. A broad set of standard mechanical characterisation tests such as tension, compression, flexural, shear and fracture are conducted on L-PBF samples [8,9]. Studies also include the effects of different processing conditions [5,10–12] and blends of virgin and reused powders [13] on the mechanical properties. However, the majority of the existing literature of the mechanical properties of PA12-based PBF components/samples has focused only on quasi-static compressive and tensile properties [4,14–18]. Material constitutive models are therefore limited to reflect only these basic properties [7]. A comprehensive understanding of fundamental properties, including shear, impact/shock, flexural, etc. of PBF polymer parts under various loading conditions that can represent the real application scenarios still requires further investigation, so

\* Corresponding authors.

E-mail addresses: [yuan.xu@eng.ox.ac.uk](mailto:yuan.xu@eng.ox.ac.uk), [yuan.xu@newcastle.ac.uk](mailto:yuan.xu@newcastle.ac.uk) (Y. Xu), [antonio.pellegrino@eng.ox.ac.uk](mailto:antonio.pellegrino@eng.ox.ac.uk) (A. Pellegrino).

<https://doi.org/10.1016/j.matdes.2023.112162>

Received 8 March 2023; Received in revised form 4 June 2023; Accepted 10 July 2023

Available online 12 July 2023

0264-1275/© 2023 The Authors. Published by Elsevier Ltd. This is an open access article under the CC BY license (<http://creativecommons.org/licenses/by/4.0/>).

as to set a foundation to make products reproducible and reliable that in the end facilitates technology transfer from a stage of rapid prototyping to product development.

The major limitation of PBF polymer parts is the inherent anisotropy due to the discontinuous deposition mechanism [6,18–20]. The stacking/building orientation of the stratified process could have a considerable effect on the mechanical properties of PBF structures as the bond strength and ductility largely depend on local process conditions. Usually the strength, stiffness, and fracture toughness are highest in the direction parallel to the direction of laser scanning and lowest in the direction perpendicular to the printing [20–22]. From the microscopic point of view, porosities resulted from crystallisation during the sintering process and their shape changes affected by re-coating can be among the main reasons that induce anisotropy. Due to the residual porosity PBF polymer parts are generally shown to have to possess poor ductility [6,11,20,23]. These microstructural peculiarities can modify a variety of mechanical responses in comparison to traditionally processed materials [24].

In the literature, most research into the anisotropy of PBF parts is limited to a quasi-static loading regime by evaluating the tensile properties of dog-bone test specimens manufactured in different directions with respect to the deposition configuration [11,12,16,17,19]. Furthermore, if altering the raster angle of the specimen with respect to the loading direction by a series of angles, a variety of combined tensile-shear stress states can be created in the localised coordinate system. In this way, some researchers [25] addressed the anisotropy and assessed the structural integrity by developing a failure envelope from the different combined loading stress states. Using the same approach, Obst et al. [26] constructed the failure envelope of L-PBF manufactured PA12 parts from the measured tensile, compressive, shear strengths, and their combinations from combined axial-torsional loading experiments. They found that the failure is strongly influenced by the interaction between stress components. Compared to conventional manufacturing methods, the anisotropic nature of AM parts can result in distinct material behaviours which brings difficulty in predicting failure and therefore hinders its application into product development without a comprehensive understanding of the mechanical properties. It is important to conduct experiments under complex loading conditions while considering different printing orientations to assess the potential anisotropy that incorporates stress interactions.

Furthermore, polyamide including PA12 is known for its excellent impact resistance. It is a popular replacement for metal parts in diverse applications from automotive or aeronautics to biomedical or defence engineering [27,28], where parts tend to engage in a highly dynamic loading environment featuring impact or vibrations. Competitive high-rate properties of additively manufactured polyamide compared to its conventionally produced counterpart is desirable in such engineering applications. Unlike metals or ceramics, polymers possess rather high sensitivity to strain rate as their strength can be double or tripled with the increasing strain rate by several orders in magnitude [29,30]. Despite the increasing number of studies on the mechanical behaviour of polymer PBF parts, research into their rate dependency is still limited [20,27,31,32]. Mehdipour et al. [20] assessed the rate dependency together with the anisotropy of L-PBF printed PA12 tensile dog-bone specimens manufactured in three build orientations; rate dependency of the tensile strength and elongation to break were observed within a low strain rate range on the order from  $10^{-3}$  to  $10^{-2} \text{ s}^{-1}$ . Cook et al. [31] conducted mechanical testing of L-PBF processed polyamide in a wide range of strain rates ( $10^{-3}$  to  $10^3 \text{ s}^{-1}$ ) to construct an Eyring plot of flow stress versus logarithm of strain rate and demonstrated a significant strain-rate dependence. This rate-dependence, often a bi-linear response at high rates, has been shown to be a material property and is due to the movement of the  $\beta$  transition to room temperature at these rates. The effects of build orientation and strain rate on the fracture toughness and failure of PA12 processed by L-PBF were investigated by Crespo and Gómez-del Río et al. [27,32]. Previous investigations have also studied

the effect of the build orientation and temperature on the mechanical response and fracture behaviour of polyamide 12 and glass filled polyamide 12 processed by selective laser sintering [18]. Other authors have used time-temperature superposition to predict the dynamic behaviour of polymers by means of experiments conducted at low strain rate at low temperature [33,34]. However, replicating the high strain rate behaviour and applying common concepts such as time-temperature superposition and rate-temperature equivalence of yield to large strains becomes challenging due to the temperature rise induced by adiabatic heating [35,36]. Moreover the principle of time-temperature superposition requires, for the investigated material, the assumption of thermorheologically simple behaviour [37]. Because of the above-mentioned challenges the literature is scarce of studies concerning the concurrent effects of strain rate and anisotropy on polymer-based L-PBF materials. Particularly, no previous study addresses the anisotropic rate dependent behaviour of additively manufactured polymers under combined dynamic loading.

In this study, the tensile-shear behaviour of L-PBF manufactured PA12 is experimentally investigated with a particular focus on the effects of strain rate dependency and build orientation induced anisotropy. A variety of stress states are assessed, including pure shear, plane strain tension, uniaxial tension, and combined tension-shear with different ratios between the tensile and shear components. The entire strain vs stress response is determined at strain rates from  $10^{-3}$  to  $10^3 \text{ s}^{-1}$ . The rate dependent ultimate stress loci are constructed in the principal stress space. A modified von Mises model is employed to predict the failure envelope and characterise the compression-tension asymmetry. The concurrent effect of the strain rate dependency and anisotropy are addressed regarding the stress-strain response, stress locus, and fracture morphology.

## 2. Materials and manufacturing

The specimen is designed as a thin-walled cylinder (Fig. 1) employed in tensile, torsional, and combined loading experiments at quasi-static and high strain rates. The ends of the specimen are shaped as octagon slots with external thread to transmit both the axial and torsional loads. The gauge section has wall thickness of 0.5 mm, internal diameter of 16.65 mm, and gauge length of 2 mm. The transition from the gauge to shoulders is shaped as fillet on both the internal and external sides, resulting in the axisymmetric cross section a dog-bone geometry.

The dimensions of the gauge section, especially the internal diameter and the external diameter, are carefully inspected as they play a critical role in the data analysis. Due to the special inner geometry of the specimen and the induced difficulty in measuring it, a WENZEL<sup>1</sup> coordinate measuring machine was employed to measure the internal diameter. The measurements indicate that the L-PBF processed PA12 specimens possess an outer diameter nearly identical to the designed dimension, while the inner diameter is slightly smaller than the designed value with an error on the order of 0.15 mm for both building orientations. This is attributed to thermal expansion/shrinkage during the L-PBF process. Despite the small discrepancy, the build orientation seems to have little influence on the critical dimensions at the gauge section. The actual measurements were used in this study. Besides, the external thread of the L-PBF specimen can match well with its counterpart. The appropriateness of the threaded connection is also demonstrated by the high-rate experimental results, which are free from spurious wave oscillations.

The EOS Formiga P110<sup>2</sup> was employed for printing the samples using a commercial polyamide powder PA2200 (PA12, melting temperature 176 °C) supplied by EOS. The built-in factory processing parameters were used for the layer-by-layer fusion of the plastic powders, shown in

<sup>1</sup> WENZEL Metromec AG, Chur, Switzerland.

<sup>2</sup> EOS GmbH Electro Optical Systems, Krailling, Germany.

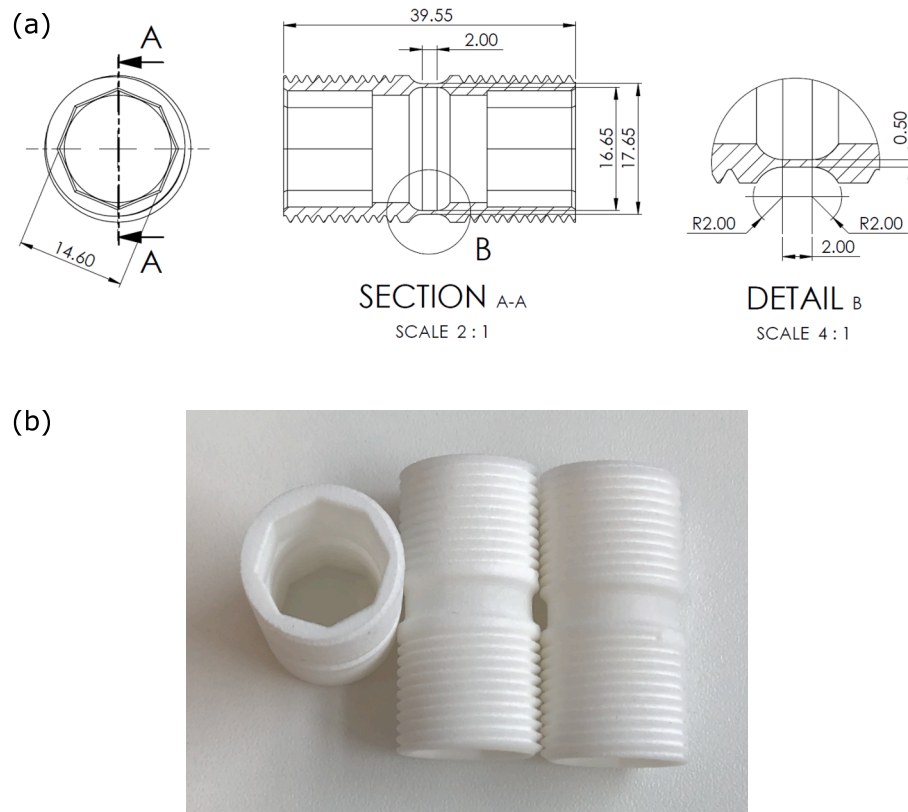


Fig. 1. Geometry of the tension-torsion specimen.

Table 1

The built-in parameters of L-PBF process.

Parameter	Value
Laser power	30 W
Particle diameter	D50 = 58 $\mu\text{m}$
Powder ratio	50/50
Powder bed temperature	170 $^{\circ}\text{C}$
Frame temperature	150 $^{\circ}\text{C}$
Layer thickness	100 $\mu\text{m}$
Energy density	3.36 J/cm <sup>2</sup>
Laser beam diameter	250–400 $\mu\text{m}$
Cooling time	>12 h

**Table 1.** Energy density, the most important parameter in PBF process as is fundamental to pore formation [11,12,14], was set to medium energy input within the well-studied range [11]. The influence of the processing parameters on the mechanical properties of PBF parts is beyond the scope of this study.

To evaluate the build orientation-induced anisotropy in the mechanical properties, specimens were fabricated in two directions such that the build direction aligns with the Y-axis or Z-axis of the sample, as illustrated in Fig. 2, referred to as Y-samples and Z-samples in this study. The influence of the laser direction and the transverse direction is not discussed herein. All the Y-samples are printed with their Z-axis aligned in the laser scanning direction.

### 3. Methodology

#### 3.1. Quasi-static experiment

Quasi-static (QS) tensile, torsional, and combined loading experiments were conducted using a Zwick/Roell Z250 screw-driven universal testing machine (Fig. 3). The tensile load was applied under

displacement control at a speed of 0.002 mm/s, while the torsional load applied at 0.05 $^{\circ}$ /s. In combined tension-torsion loading experiments, the proportion of the tensile and torsional loading was varied via altering the respective loading velocities. Two combinations (0.002 mm/s and 0.06 $^{\circ}$ /s, 0.003 mm/s and 0.03 $^{\circ}$ /s) were selected to obtain shear-dominated and tension-dominated biaxial stress states, respectively.

The applied force and torque were recorded via the respective resistive load cells, Zwick Force 100 kN and Zwick Torque Transducer 100 Nm. The full-field of tensile and shear displacements were retrieved, using Digital Image Correlation (DIC) techniques, from the macroscopic deformation that was video-recorded by four synchronised iDs<sup>3</sup> UEye USB 3.0 Cameras (Fig. 3). Images were captured at a frame rate of 1 Hz via a CMOS sensor with a resolution of 2456  $\times$  2054 pixels. A fine grey-scale speckle pattern was applied to the surface of the specimen to favour the DIC analysis. The quality of the speckle pattern was verified using the mean intensity gradient (MIG) index [38,39]. The MIG index of the speckled region of interest for all experiments was calculated in the range from 25 to 45, which is above the critical value 20 associated with a mean bias error of displacement of less than 1 %. The commercial software LaVision DaVis was used to measure axial and shear strain within the gauge section of the specimen.

#### 3.2. High strain rate experiment

High-rate (HR) tensile, torsional, and combined loading experiments were carried out using a combined Tension-Torsion Hopkinson Bar (TTHB) system [40] that was designed and developed at the Impact Engineering Laboratory, University of Oxford. The TTHB system is schematically shown in Fig. 4a, essentially comprised of an incident bar,

<sup>3</sup> IDS Image Development Systems GmbH.

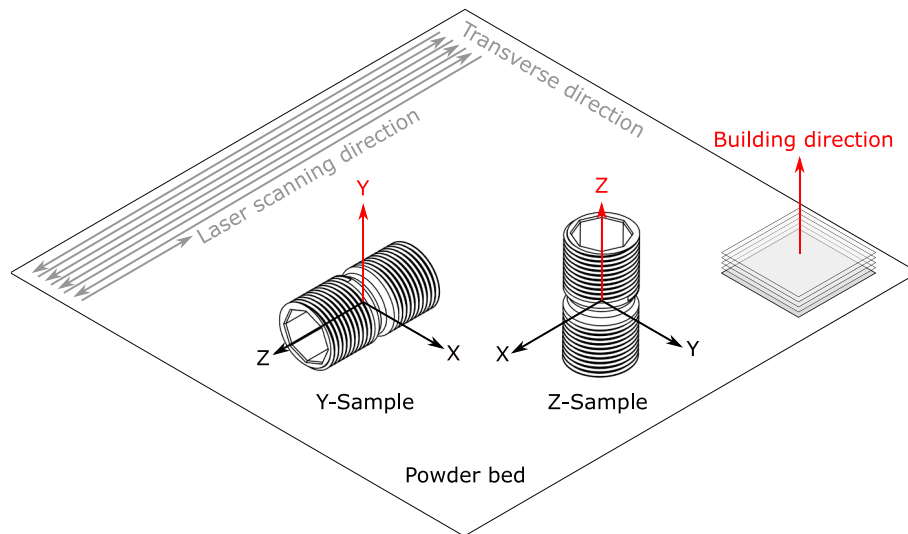


Fig. 2. PBF build job configuration with specimens manufactured in Y-direction and Z-direction.

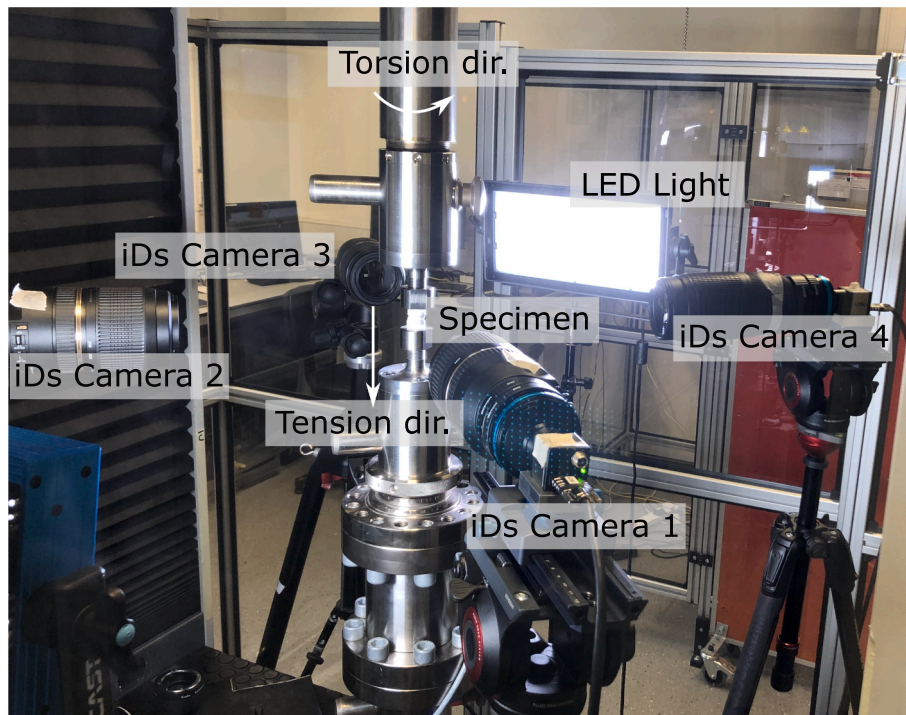


Fig. 3. Quasi-static testing setup.

a transmitted bar, with the specimen sandwiched in between, a rapid release clamp station, a tensile and torsional loading unit, and a data acquisition system. The working principle and the technical specification of the TTHB, as well as data interpretation of a typical TTHB experiment, are elaborated in previous work [40–43] and is not detailed here.

The experimental setup and the data acquisition system employed in this study are presented in Fig. 4b. Apart from a set of strain gauges that measure the longitudinal and shear stress waves propagating along the bars and through the specimen, the data acquisition system consisted of two synchronised Photron SA-5 high-speed cameras that were triggered by the incident wave signal. The high-speed deformation of the specimen was captured at a frame rate of  $10^5$  Hz with a resolution of  $320 \times 192$  pixels. The high-rate strain variation within the gauge section of the

specimen was subsequently measured from the footage via DIC techniques. The history of the tensile and torsional loads was calculated using one-dimensional wave theory based on D'Alembert's solution [44].

### 3.3. Evaluation of stress and strain

#### 3.3.1. Average engineering stress and strain

In a combined loading test, the nominal axial stress  $\sigma$  and shear stress  $\tau$  on the cross-section of the thin-walled tube gauge of the specimen are calculated from the axial force  $F$  and torque  $T$  measured from experiments via Eqs. (1)–(2) by assuming homogeneous stress distribution given the small thickness-to-diameter ratio:



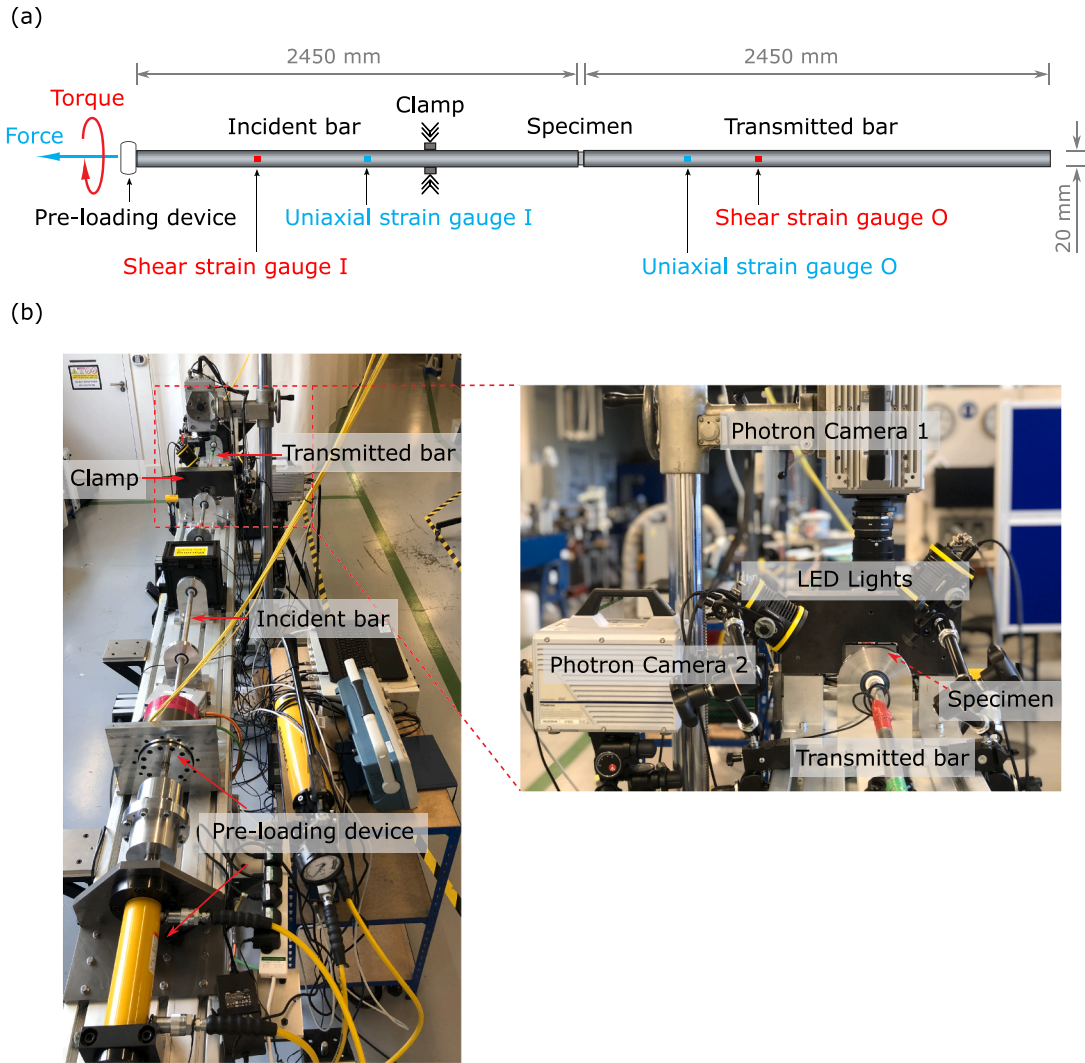


Fig. 4. High strain rate testing setup.

$$\sigma = \frac{F}{A} \quad (1)$$

$$\tau = \frac{Tr}{J} \quad (2)$$

where,  $A$ ,  $r$ , and  $J$  denote the cross-section area, radius, and polar moment of inertia of the thin-walled tube, respectively.

The nominal axial strain  $\epsilon$  and the nominal shear strain  $\gamma$  for a given gauge length  $l_0$  can be averaged by Eqs. (3)–(4):

$$\epsilon = \frac{dU}{l_0} \quad (3)$$

$$\gamma = \frac{dV}{l_0} \quad (4)$$

where,  $dU$  is the axial displacement and  $dV$  the tangential displacement of the initial length  $l_0$  of the gauge section. Illustrations of the stress and strain can be found in previous work [42].

### 3.3.2. Stress state

The parameter biaxial loading angle  $\beta$  is introduced to describe the proportion of the tension and torsion in the combined loads, defined as Eq. (5). Among the multiaxial loading cases implemented in this study,

the biaxial loading angle falls within the range of  $0^\circ \leq \beta \leq 90^\circ$ , in which  $\beta = 0^\circ$  represents torsional loading, while  $\beta = 90^\circ$  indicates tensile loading.  $0^\circ < \beta < 90^\circ$  corresponds to any combinations of the tensile and torsional loads, in which  $\beta$  approaching  $0^\circ$  indicates shear-dominated combined loading while  $\beta$  approaching  $90^\circ$  suggests a tension-dominated case.

$$\beta = \tan^{-1} \frac{\sigma}{\sqrt{3}\tau} \quad (5)$$

Given the thin-walled tube geometry, the stress state  $\sigma$  at an arbitrary point within the gauge section is approximated as Eq. (6), assuming plane strain in the circumferential direction and plane stress in the radial direction.

$$\sigma = \begin{bmatrix} 0 & 0 & 0 \\ 0 & \nu'\sigma & \tau \\ 0 & \tau & \sigma \end{bmatrix} \quad (6)$$

where,  $\sigma$  and  $\tau$  refer to the axial stress and shear stress calculated from the exerted loads using Eqs. (1) and (2).  $\nu'$  denotes the effective Poisson's ratio, which equals to (i) the material Poisson's ratio for elastic deformation and (ii) 0.5 during plastic flow assuming incompressibility of the material.

The stress state is quantified by stress triaxiality  $\eta$  that is defined as

the ratio of the hydrostatic stress  $\sigma_m$  over the von Mises equivalent stress  $\sigma_e$ :

$$\eta = \frac{\sigma_m}{\sigma_e} \quad (7)$$

where,  $\sigma_m = \text{Tr}(\sigma)/3 = I_1/3$  with  $\sigma$  the stress tensor and  $I_1$  the first invariant of  $\sigma$ ;  $\sigma_e = \sqrt{3/2 s : s} = \sqrt{3J_2}$  with  $s$  the deviatoric stress tensor,  $s = \sigma - \sigma_m \mathbf{I}$ , and  $J_2$  the second invariant of  $s$ . Lode angle parameter  $\bar{\theta}$  is also employed to characterise the deviatoric stress state,

$$\bar{\theta} = 1 - \frac{2}{\pi} \arccos \left( \frac{27}{2} \frac{\det(s)}{\sigma_e^3} \right) \quad (8)$$

### 3.3.3. Build direction

A schematic representation of the distinct layer-by-layer structures of Y-specimen and Z-specimen are shown in Fig. 5a. The samples are idealised as hollow cylinders, and the thickness-to-diameter ratio does not reflect the real scale. The representative volume of the Z-specimen possesses an identical layered structure at any angle  $\theta$  along the circumference. By contrast, the layered structure varies periodically along the circumference of the Y-specimen. The structures of three representative volume sections are shown at angles of  $0^\circ$ ,  $45^\circ$ ,  $90^\circ$ .

When subjected to an axial force  $F$  and a torque  $T$ , the Y- and Z-specimens yield different stress/strain states with respect to the layer-by-layer structures, as depicted in Fig. 5b. Two monotonic loading scenarios, tensile loading and torsional loading, are taken as examples. Combined tension–torsion loading is assumed as a superposition of these two cases.

Given the unvaried layered structure of the Z-specimen, the stress state of any representative volume Z- $\theta$  remains the same. When loaded by tension, the axial tensile stress  $\sigma$  of the volume Z- $\theta$  is perpendicular to the layers while the circumferential stress  $\nu'\sigma$ , resulted from the lateral constraint, is parallel to the layers. When loaded by torsion, the shear stress acts in between the layers.

However, the stress state of Y-specimen is more complicated. When loaded by tension, the axial tensile stress  $\sigma$  of volume Y- $0^\circ$  is parallel to the layers, to which the circumferential stress  $\nu'\sigma$  is perpendicular. For

volume Y- $90^\circ$ , both the axial stress and the circumferential stress are parallel to the layers. When loaded by torsion, the stress state of volume Y- $0^\circ$  is equivalent to that of Z- $\theta$ , while the shear stress of volume Y- $90^\circ$  is in the plane of the layers.

## 4. Results and discussion

The tensile-shear behaviours of L-PBF PA12 are discussed in this section, to reveal the effects of the build direction, strain rate, and multiaxial loading. A summary of the quasi-static behaviour of the Y- and Z-specimens measured at different tensile-shear stress states is detailed in Table 2, while the high-rate responses are summarised in Table 3.

Fig. 6 plots the theoretical range of stress states achievable with the specimen geometry and those obtained from the experiments in quasi-static and high-rate loading regimes. Given the plane stress conditions of the specimen, the stress triaxiality  $\eta$  relates to the Lode angle parameter  $\bar{\theta}$ , at the same time, both parameters correspond to the biaxial loading angle  $\beta$ , shown as the solid lines in Fig. 6a and b, respectively. The experimentally achieved stress states at the ultimate point are depicted as marks various shapes and colours that distinguish the relevant strain rate and the build direction of the specimen.

The torsion on tubular samples ( $\beta = 0^\circ$ ) corresponds to a pure shear stress state which is characterised by  $\eta = 0$  and  $\bar{\theta} = 0$ . The same Lode angle parameter  $\bar{\theta} = 0$  is associated with tension on tubular samples ( $\beta = 90^\circ$ ) but yielding a stress state of plane strain tension  $\eta = 0.577$ . A combined tension–torsion loading is characterised by  $0^\circ \leq \beta < 90^\circ$ , in which  $\beta = 39^\circ$  is equivalent to a stress state of uniaxial tension on dog-bone samples  $\eta = 1/3$  and  $\bar{\theta} = 1$ . It is therefore reasonable to define in a tensile-shear stress state that the tensile component predominates when  $39^\circ < \beta < 90^\circ$  while the shear counterpart prevails when  $0^\circ < \beta < 39^\circ$ . It is shown that a wide range of stress states can be achieved using the thin-walled tubular specimen geometry. A variety of stress states are covered in this study, including pure shear, plane strain tension, uniaxial tension, and combined tension-shear characterised by different weights of the tensile and shear components. Such highly discriminating tests contribute to assessing the effects of stress triaxiality and the deviatoric

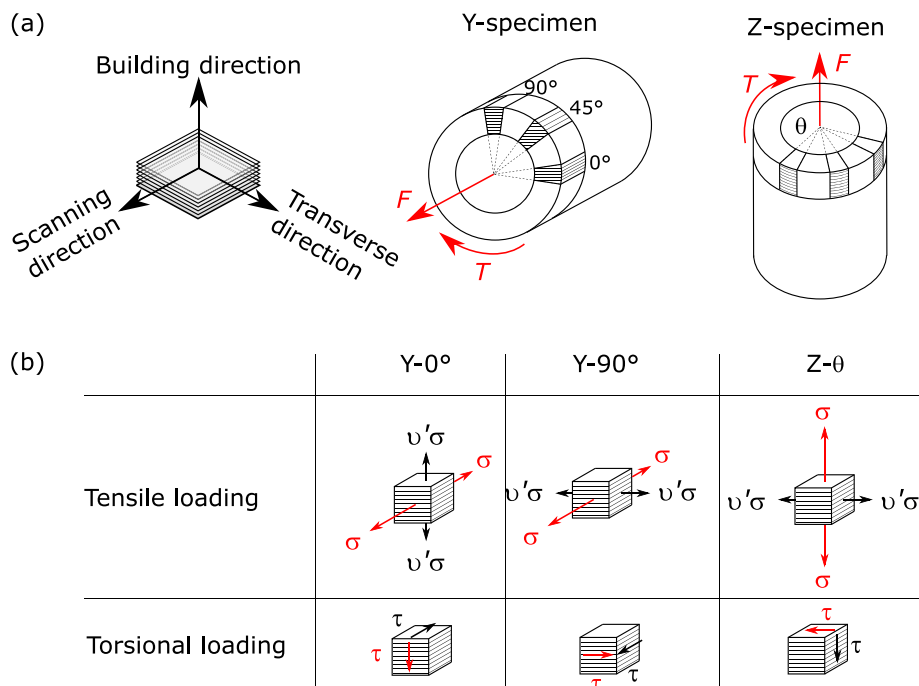


Fig. 5. Effect of the build direction on the stress state: (a) schematic of the various layer-by-layer structure of specimens built up in Y- and Z- directions; (b) simplified stress states under tensile loading and torsional loading.

**Table 2**

A summary of the quasi-static mechanical behaviours of the Y- and Z-specimens.

Loading type	Specimen no.	Biaxial loading angle (°)	Young's modulus (GPa)	Shear Modulus (GPa)	Ultimate strength		Fracture strain	
					Tension (MPa)	Shear (MPa)	Tension (%)	Shear (%)
Tension	Y1	90	2.18 ± 0.92	–	47.5	–	26.6	–
	Y2	90	1.78 ± 0.40	–	45.3	–	21.9	–
	Z7	90	1.59 ± 0.06	–	44.6	–	33.0	–
	Z8	90	1.63 ± 0.15	–	45.1	–	32.9	–
Combined Tension-Torsion	Y16	50	–	–	30.4	14.6	24.5	41.9
	Y17	48	–	–	30.1	15.9	27.8	47.4
	Y3	28	–	–	22.6	24.2	28.3	120.8
	Y4	27	–	–	21.3	23.7	21.6	109.1
	Z16	49	–	–	30.9	15.6	27.0	45.5
	Z17	48	–	–	31.6	16.2	46.8	73.8
	Z11	28	–	–	23.0	25.5	38.6	158.5
	Z15	23	–	–	17.2	23.1	43.0	183.3
Torsion	Y11	0	–	0.50 ± 0.04	–	35.9	–	*
	Y12	0	–	0.59 ± 0.03	–	35.2	–	225.8
	Z9	0	–	0.51 ± 0.02	–	33.0	–	*
	Z10	0	–	0.71 ± 0.03	–	32.0	–	185.6
	Z14	0	–	0.80 ± 0.07	–	34.9	–	175.0

Note: 1. (–) not applicable; (\*) no fracture observed prior to failure.

2. Young's and shear moduli are provided as an average value with a standard deviation, given that four moduli per specimen are obtained from the overall stress and four strain measurements on the circumference.

**Table 3**

A summary of the high-rate mechanical behaviours of the Y- and Z-specimens.

Loading type	Specimen no.	Biaxial loading angle (°)	Strain rate		Ultimate strength		Fracture strain	
			Tension (s <sup>-1</sup> )	Shear (s <sup>-1</sup> )	Tension (MPa)	Shear (MPa)	Tension (%)	Shear (%)
Tension	Y6	90	128	–	54.9	–	3.3	–
	Y14	90	205	–	53.5	–	7.5	–
	Z13	90	140	–	54.9	–	6.5	–
	Z12	90	171	–	56.5	–	7.2	–
	Z1	90	456	–	60.8	–	9.7	–
Combined tension-torsion	Y7	40	136	331	38.6	26.9	3.4	7.7
	Y8	40	287	747	40.4	27.5	5.9	16.6
	Z3	31	309	2001	24.4	23.2	12.6	78.2
	Z4	29	358	3033	30.5	31.6	8.7	55.3
Torsion	Y9	0	–	3645	–	42.1	–	91.4
	Y10	0	–	2388	–	41.1	–	123.5
	Z5	0	–	233	–	26.6	–	*
	Z18	0	–	2190	–	30.2	–	80.1
	Z6	0	–	2495	–	31.1	–	84.7

Note: (–) not applicable; (\*) no fracture observed prior to failure.

stress state on the deformation and failure of the material under consideration.

#### 4.1. Quasi-static experiments

The typical engineering stress–strain relationships of Y- and Z-specimens under quasi-static monotonic tensile loading and monotonic torsional loading are presented in Fig. 7. The shaded curves are determined by different strains measured from the four cameras surrounding the specimen. Both the tensile and shear stress–strain curves show classic viscoplastic behaviours of polymeric materials that go through elastic deformation, yielding, viscoplastic flow and the final failure. During the viscoplastic deformation, PA12 experiences minor strain hardening and then strain softening that features strain localisation and microscopic voids prior to the final fracture or failure. The nominal fracture point is defined as the 10% load drop from the ultimate stress

point, marking the end of the curves. The progressive deformation is demonstrated in Figs. 8–10 through five representative stages including the pristine, yielding point, ultimate point, 10% load drop, and the final fracture.

In the case of monotonic tensile loading, the Y-sample is characterised with almost identical ultimate strength as the Z-sample, 45.3 and 44.6 MPa, respectively. Noticeable anisotropy in elongation at break could be readily seen as the former falls within the range of 21%–25%, significantly smaller than that of the later, approximately 33%. The insensitivity of the strength to the build direction has been reported by the powder supplier and other researchers [8,16,45] using ASTM or ISO standards for characterising uniaxial tensile properties of plastics in a quasi-static loading regime [46–48]. Note that dog-bone specimens are adopted in these test methods to achieve a uniaxial tensile stress state, from which a smaller elongation at break is measured within the range of 4–15% on specimens manufactured in the longitudinal direction (Z-

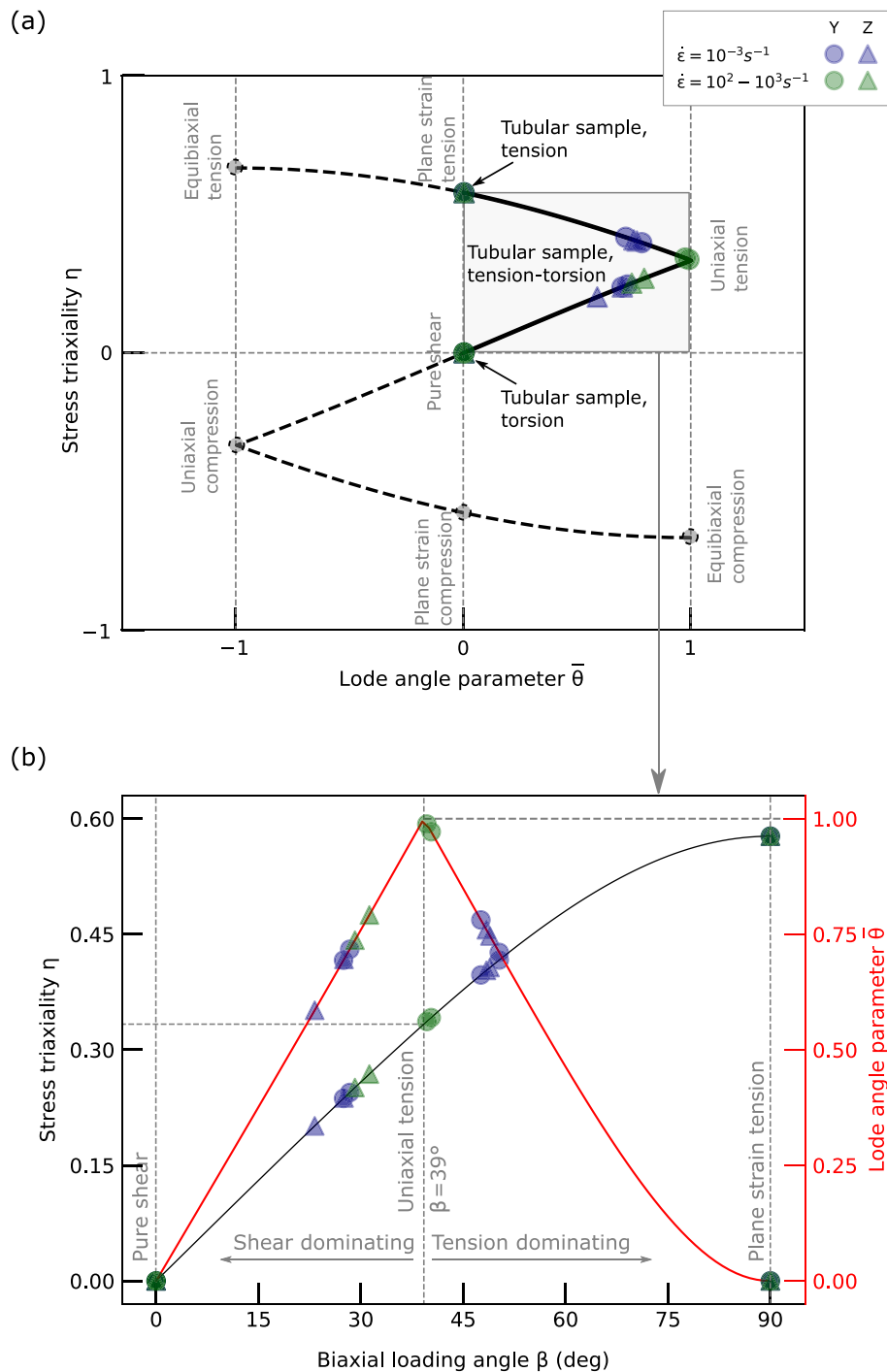


Fig. 6. Theoretical range of stress state achievable with the specimen geometry and experimental data: (a) 2D plane ( $\bar{\theta}, \eta$ ); (b) 2D plane ( $\beta, \eta$ ) and ( $\beta, \bar{\theta}$ ).

direction) while a considerably larger value of 20–32% is reported on specimens built up in the thickness or lateral direction (X- or Y-direction) [16,45,49]. The variance of the measured elongation at break in the literature could be related to different mechanisms of crystallisation kinetics from AM processing. The varied degrees of crystallisation among the feedstock, inter-layer boundaries and merged new layers would result in distinct microstructures in the AM polymer part and consequently have a profound influence on its mechanical properties [50]. Higher crystallinity leads to higher volume of shrinkage during the fusion process, which brings about inherent pores and voids, resulting in brittleness of the L-PBF parts [49,51]. The contradictory dependence of the elongation at break on the build direction observed in this study

might also be attributed to the state of plane strain tension in the thin-walled tubular specimen (see Fig. 5) whereas uniaxial tension is considered in the dog-bone sample.

In monotonic shear loading, both the Y- and Z-samples exhibited almost the same ultimate shear strength, 35.2 and 34.9 MPa, respectively. Similar strain at break could be seen from both specimens, despite that the Y-specimen deformed and fractured with more heterogeneous distribution of shear strain along its circumference.

The effect of the build direction is further observed on the strain distribution around circumference of the cylindrical samples, as indicated by the different strain ranges of the Y- and Z- specimens at a given stress level. Fig. 7a shows a narrow strip that envelopes the tensile



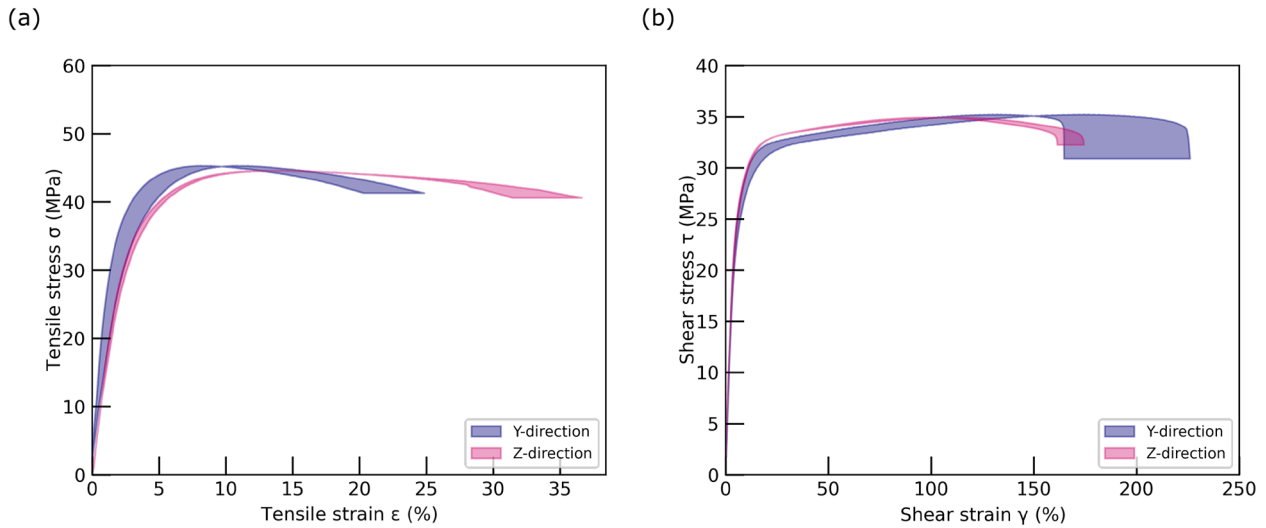


**Fig. 7.** Engineering stress–strain relationship under (a) monotonic tensile loading (#Y2 vs #Z7), and (b) monotonic torsional loading (#Y12 vs #Z14), at a quasi-static strain rate. The shaded curves are determined by different strains measured from the four cameras surrounding the specimen (see Fig. 3).

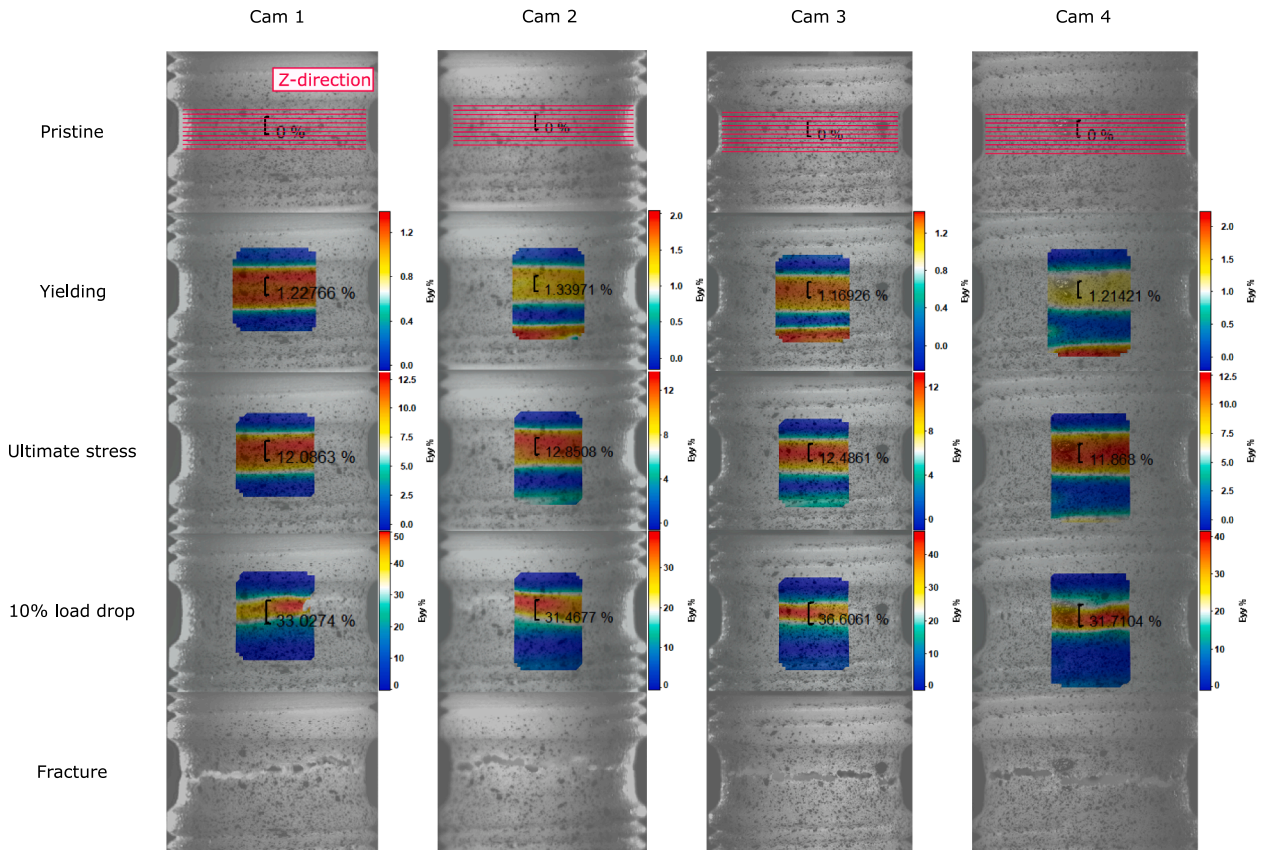


**Fig. 8.** Evolution of engineering axial strain of Z-specimen (#Z7) under monotonic tensile loading.

stress–strain curves of the Z-sample up to the ultimate point. Verified by Fig. 8, this indicates a high level of homogeneous distribution of the axial strain, thanks to the constant layered structure of the Z-specimen with respect to the stress state (Fig. 5b). After the ultimate point, the strains start to differ from each other, plausibly due to the strain localisation and evolution of microscopic voids and cracks. By contrast, the wide band of the tensile stress–strain curves of the Y-sample demonstrates varied axial strains along the circumference, from the elastic deformation till the nominal fracture point (see Fig. 9). In addition to the

strain localisation after the ultimate point, the anisotropy of the strain is attributed to the varying layered structures along the circumference of the Y-specimen with respect to the stress state (Fig. 5b). Since the layered structure varies at a cycle of  $\pi$ , similar strain values are measured from the opposite sides of the samples (Fig. 9). Another underlying reason for the strain anisotropy might be the different extents of shrinkage from the sequential cooling process of the melted powder layers. The dimensional measurement of the Y-specimens shows that the axial length slightly increases as the layers build up, and then decreases at

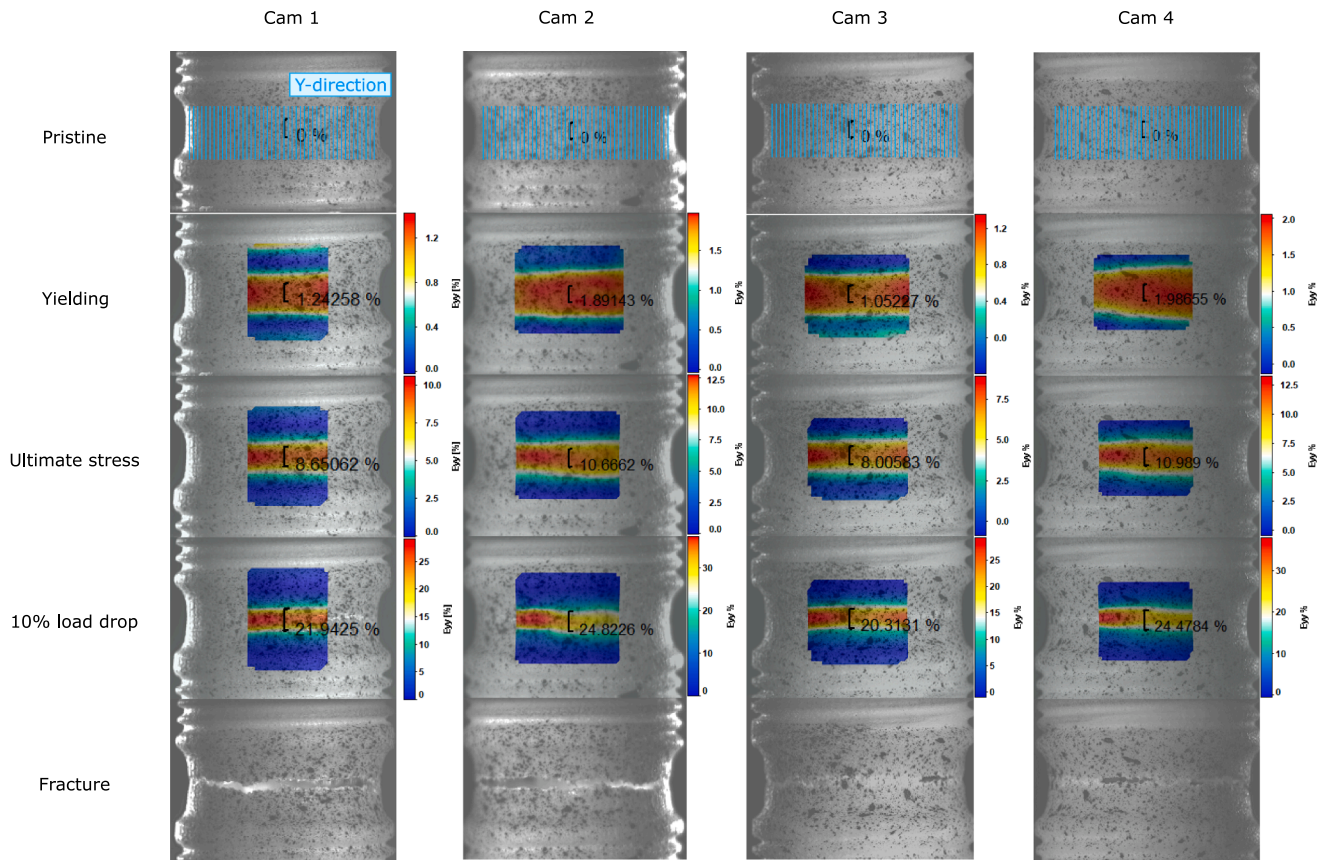


Fig. 9. Evolution of engineering axial strain of Y-specimen (#Y2) under monotonic tensile loading.

the top of the fused part, reaching the maximum length in the middle (with a standard deviation nearly 0.1 mm). Furthermore, Figs. 8 and 9 reveal nearly straight fracture rather than wavy fracture of the Z-specimen which indicates multi-layer crack propagation.

Similar to the case of the tensile loading, when subjected to monotonic torsional loading, the Z-specimen is characterised by homogeneous shear strain along the circumference, due to the constant layered structure under shear. The Y-specimen shows a heterogeneous distribution of the shear strain since the yielding point, which might be again attributed to the slightly varying axial length of the specimen and the altering layered structures with respect to the shear stress state. It is worth noting from Fig. 5b that, the layered structure of Y-0° in a shear stress state is equivalent to that of Z-θ. As a result, the Y-specimen fails at a shear strain range that covers the shear strain to failure of the Z-specimen (Fig. 7b). Fig. 10 illustrated more appreciable buckling of the Z-specimen than that of the Y-specimen after the ultimate stress point is reached.

Consequently, the measurement of Young's modulus is affected by the build direction. Young's modulus obtained from the overall stress and the four local strain measurements of Y-samples gives higher deviation than that of Z-samples, as shown in Table 2. The average value of Young's modulus of both Y- and Z- specimens is approximated as 1.79 GPa, comparable with the isotropic Young's modulus provided by the supplier, 1.70 GPa in Y and Z directions. The measurement of the shear modulus of Y- and Z- samples gives an average value of 0.62 GPa.

In the following analysis, only the strain obtained from the camera that captured the first crack initiation is used.

Fig. 11 compares the engineering stress and strain of Y- and Z-specimens at four representative stress states, including plane strain tension ( $\beta = 90^\circ$ ), tension-dominated combined tension-shear ( $\beta = 48^\circ$ ), shear-dominated combined tension-shear ( $\beta = 28^\circ$ ), and pure shear ( $\beta = 0^\circ$ ). The solid lines denote the responses of Y-specimens, while the

dashed lines represent Z-specimens. The progressive change of the line colour from navy to violet-red indicates the varying weight of the tensile and torsional components in the combined loads. Labels of all the curves are described in the legend of Fig. 11d.

It is shown from the engineering stress-strain curves in tension (Fig. 11a) and shear (Fig. 11b) that, as the biaxial angle  $\beta$  decreases, namely the shear becomes predominant in the multiaxial stress states, the ultimate tensile strength reduces while the ultimate shear strength is enhanced, and vice versa. The effect of stress triaxiality on the strain at failure shows an increasing trend in both the tensile and shear strain as with the shear component prevailing in the combined loads.

The trajectories of the tensile strain and shear strain (Fig. 11c) show a constant ratio between the strain components in a given multiaxial loading case. The loading paths in terms of the tensile stress and shear stress (Fig. 11d) demonstrate nearly proportional evolution of the stress components throughout the multiaxial loading. The proportional development of the tensile and shear strain/stress indicate that a constant triaxiality was guaranteed during the tensile-torsional loading and that the biaxial angle  $\beta$  calculated from the maximum stress components is valid throughout the loading process.

#### 4.2. High-rate experiments

The behaviours of Z-samples are presented herein to demonstrate the representative responses of L-PBF PA12 subjected to high-rate monotonic tensile loading and torsional loading, as shown in Fig. 12 and Fig. 13, respectively. In a typical TTHB experiment, the time history of the force or torque measured in the transmitted bar can represent the load on the transmitted end of the specimen through a time shift of the recorded strain gauge data given the distance of the strain gauge on the bar. Whereas the force or torque measured in the incident bar comprises a few stages if the strain gauge is located within the clamped section of



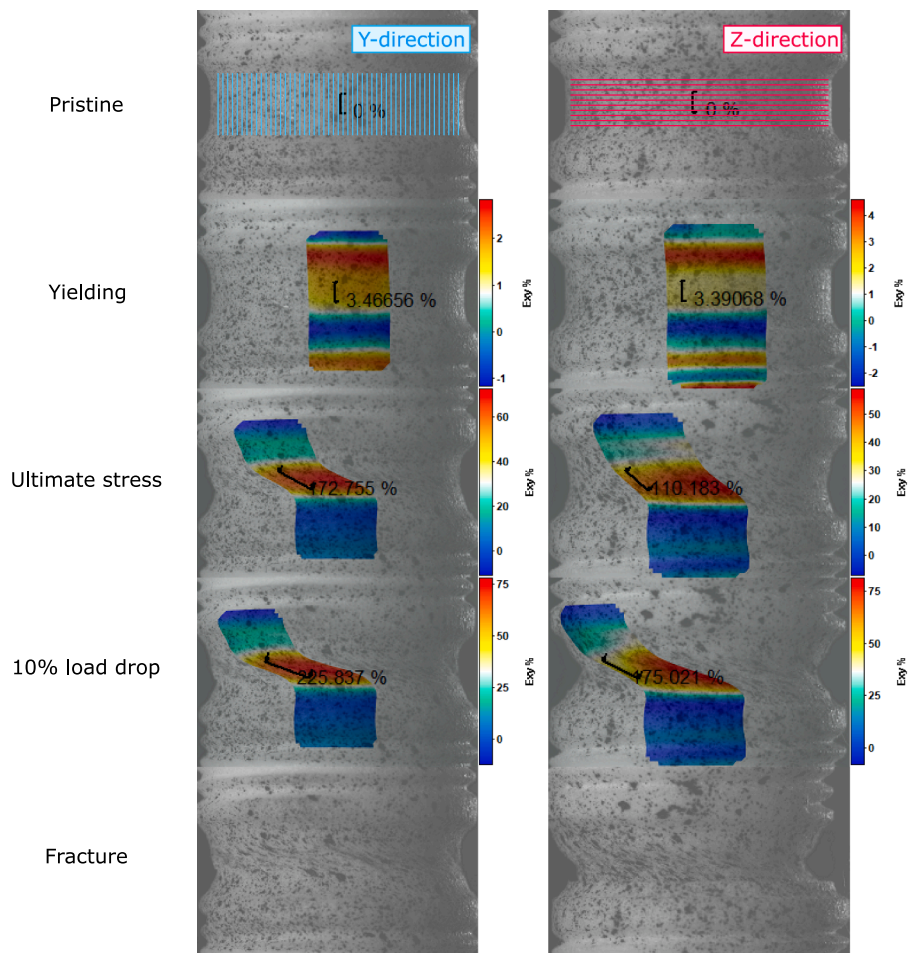


Fig. 10. Evolution of engineering shear strain of Y-specimen (#Y12) and Z-specimen (#Z14) under monotonic torsional loading.

the incident bar as illustrated in the presented experiment setup (Fig. 4a).

In tension (Fig. 12a), the curves *Stored/released wave-Longitudinal* and *Transmitted wave-Longitudinal* denote the time histories of the forces measured in the incident and transmitted bars, respectively. The initial force of the incident curve indicates the amount of *stored energy*; the subsequent decrease by half of the stored energy corresponds to the initiation of the longitudinal wave via the clamp release (*Wave release*); then the wave interacted with the specimen and was partially transmitted to the transmitted bar while the rest was reflected back into the incident bar (*Wave loading till specimen failure*); in this regime, the force history recorded by the strain gauge in the incident bar represents the sum of the incident wave and of the reflected wave, i.e. the force applied on the incident end of the specimen. More details on the wave analysis, including  $x-t$  and  $v-t$  diagrams of the wave propagation in a typical TTHB experiment can be found in [42].

It is observed that, in the high rate loading regime, equilibrium was achieved at a time of the order of  $160 \mu\text{s}$ , which corresponds to a nominal tensile strain of 1.6 %, shown as a white circle in Fig. 12a-b. During dynamic equilibrium, the nearly linear slope of the strain history approximates a constant strain rate of  $171 \text{ s}^{-1}$ . The wave oscillations prior to  $160 \mu\text{s}$  is attributed to the initial slack in the thread coupling between the specimen and the loading bars. We conclude that the measured high-rate stress-strain curves are valid from the point of achieving dynamic equilibrium for all the high-rate experiments. Apparent strain hardening can be identified until the elongation at break of 7.2 %. The ultimate strength is measured at 56.5 MPa, indicating positive strain rate dependence.

In torsion (Fig. 13a), the torques applied on the incident and transmitted ends of the specimen initially differed in the regime of wave loading, due to the slack in the mechanical octagonal coupling between the specimen and the loading bars and then the higher acceleration of the incident bar than that of the specimen with a lower wave impedance; however, the torques equalise at a time on the order of  $250 \mu\text{s}$ , corresponding to a nominal shear strain  $\epsilon_{xy} = \gamma_{xy}/2 = 9.4\%$ . The specimen went through large shear deformation, and during dynamic equilibrium, at a constant shear strain rate of  $2495 \text{ s}^{-1}$ . The valid part of the shear stress-strain curve (Fig. 13b), where dynamic equilibrium was satisfied, shows strain hardening and, after the ultimate point, minor strain softening until the failure strain at 85 %. The ultimate shear strength is measured at 31.1 MPa, slightly lower than the quasi-static counterparts.

The effect of the strain rate and the build direction on the tensile and shear behaviours of L-PBF PA12 is summarised in Fig. 14 by comparing the engineering stress-strain curves of Y- and Z- specimens measured from quasi-static and high-rate monotonic loading tests. Apparent rate dependence is shown from the tensile stress-strain curves of both Y- and Z- specimens (Fig. 14a). The increasing strain rate enhanced ultimate strength but significantly reduced elongation at break. A similar level of rate dependence on tensile samples was also observed, at a lower strain rate range in [20]. The tensile properties seem to be unaffected by the different printing orientations. However, the anisotropy in fracture strain is barely affected by the strain rate, as shown by the smaller fracture strain of the Y-specimen compared to that of the Z-specimen at both quasi-static and high strain rates. In shear (Fig. 14b), the higher shear ultimate strength and reduced shear fracture strain are observed from the Y-samples as the strain rate increases, similar to the rate

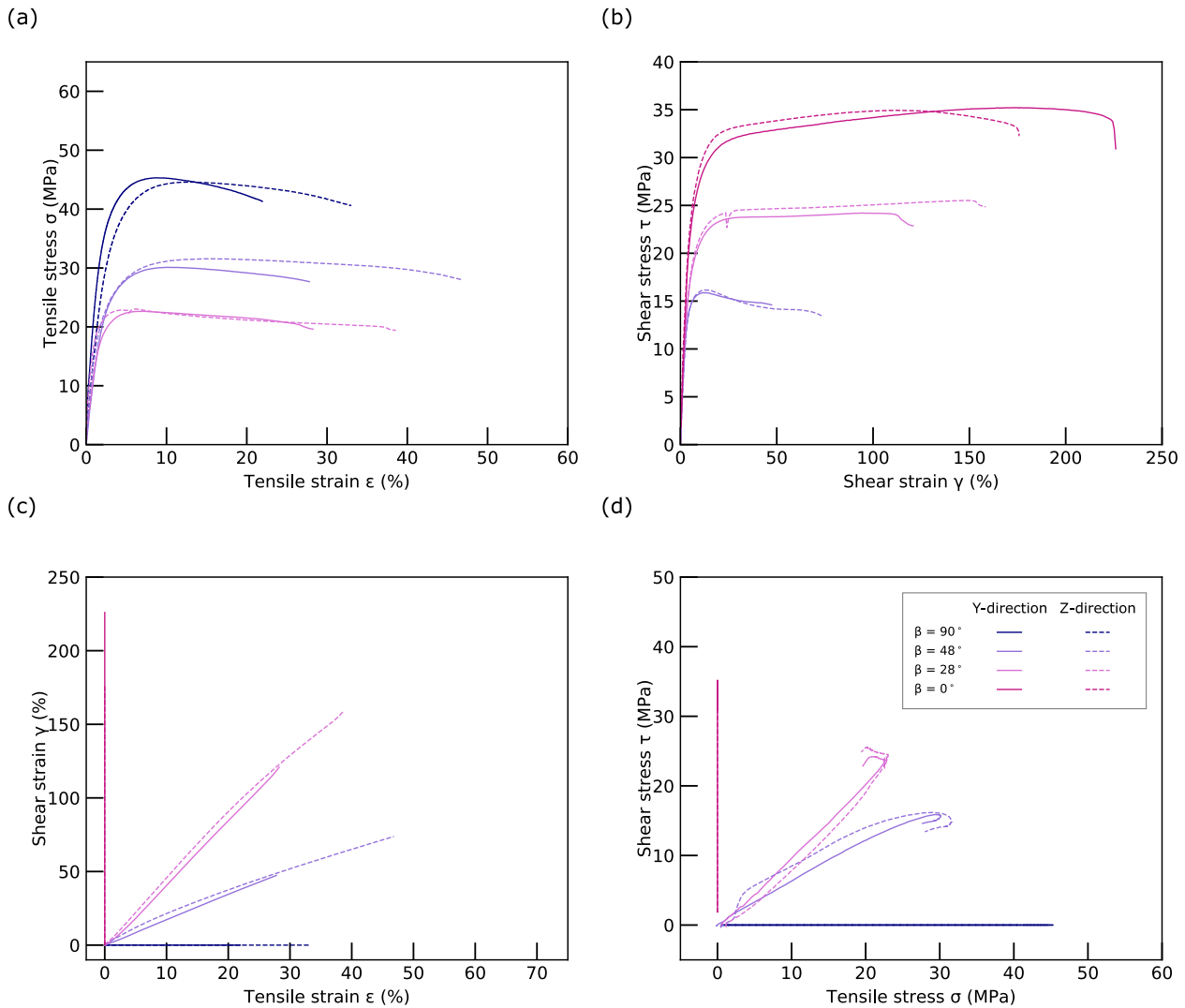


**Fig. 11.** Typical responses at different tensile-shear stress states at a quasi-static strain rate: engineering stress–strain curves in (a) tension and (b) shear, along with the trajectories of (c) shear strain versus tensile strain and (d) shear stress versus tensile stress.

dependence of the tensile strength and elongation at break. By contrast, the ultimate shear strength of the Z-sample exhibits strain rate insensitivity, which is therefore significantly lower than that of the Y-sample. Again, the strain rate never changes the effect of the build direction on the fracture strain. The Y-specimen went through larger shear deformation until the fracture than Z-specimens, at both quasi-static and high strain rates.

The high-rate engineering stress and strain of Y- and Z- specimens at three representative stress states are compared in Fig. 15, including plane strain tension ( $\beta = 90^\circ$ ), combined tension-shear ( $\beta = 40^\circ$  or  $31^\circ$ ), and pure shear ( $\beta = 0^\circ$ ). The progressively changing colour of the lines from dark green to blue indicates the different contribution of the tensile and torsional components in the combined loads. The solid lines represent the behaviours of Y-specimens, while the dashed lines are associated with Z-specimens. Labels of all the curves are detailed in the legend of Fig. 15d.

Similar to the tensile-shear behaviours in the quasi-static loading regime, the engineering stress–strain curves at high strain rates display the same biaxial loading effect on the ultimate strength and strain at break, in terms of tension (Fig. 15a) and shear (Fig. 15b). As the shear component is prevailing in the multiaxial stress states (i.e., the biaxial angle  $\beta$  decreases), the ultimate tensile strength decreases while the ultimate shear strength increases, and vice versa; both the tensile and

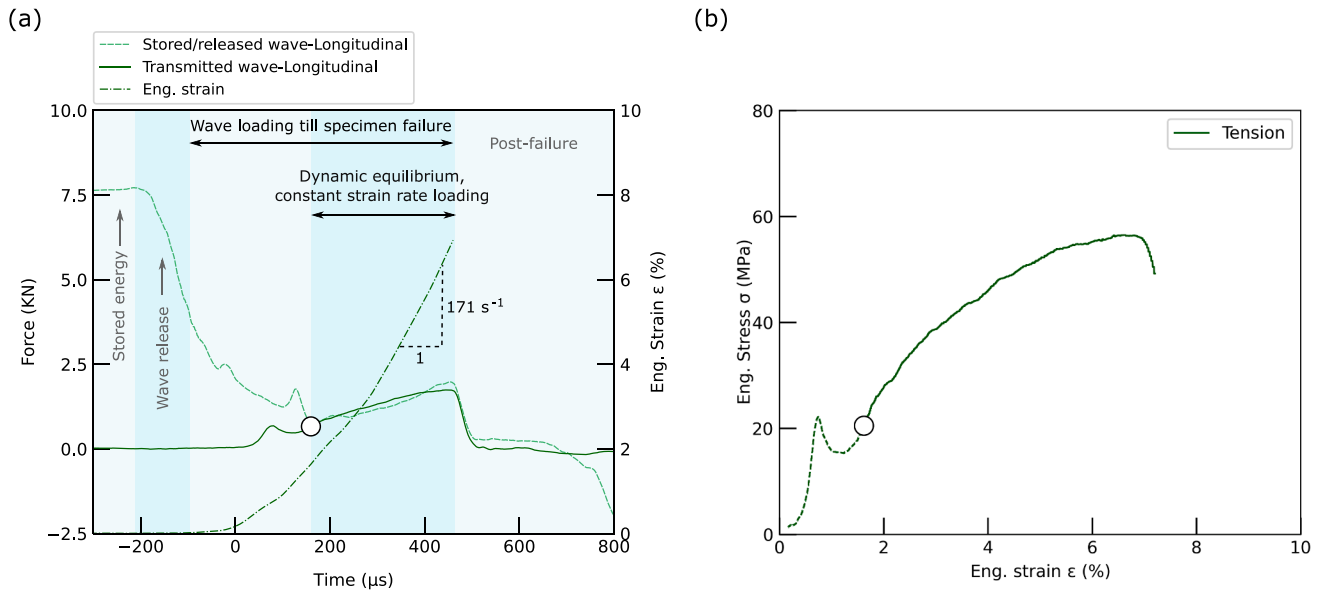
shear strain at break increase with the predominant shear in the combined loads.

Fig. 15c demonstrates that apparent proportional development between the tensile strain and shear strain is obtained under high-rate combined tension–torsion loading. The nearly constant ratio between the shear strain over the tensile strain is attributed to the constant strain rate loading achieved in the high-rate experiments using the TTHB testing method. The trajectories of the tensile stress and shear stress (Fig. 15d) are somehow entangled due to stress wave oscillations at the beginning of loading. An approximately constant ratio between shear stress and tensile stress is reached once the initial oscillations disappear.

#### 4.3. Ultimate stress locus

The measured ultimate stresses are summarised in shear versus tensile stress space (Fig. 16) to observe the evolution of the failure locus as the strain rate increases from low to high under the effect of the build direction. The low strain rate relates to a nominal quasi-static rate of  $10^{-3} \text{ s}^{-1}$ . The high strain rates achieved are on the order of  $10^2$  to  $10^3 \text{ s}^{-1}$  and labelled next to the individual data point (parentheses denote the strain rate associated with the Y-specimen, while square brackets the Z-specimen). Apparent rate dependence is observed from the failure locus of the Y-specimen, while the influence of the strain rate on that of the Z-





**Fig. 12.** High-rate monotonic tensile experiment of specimen #Z12: (a) time histories of the forces measured in the incident and transmitted bars, along with the history of the engineering tensile strain from DIC analysis; (b) tensile engineering stress–strain curve. Dynamic equilibrium was achieved from the point indicated by the white circle.

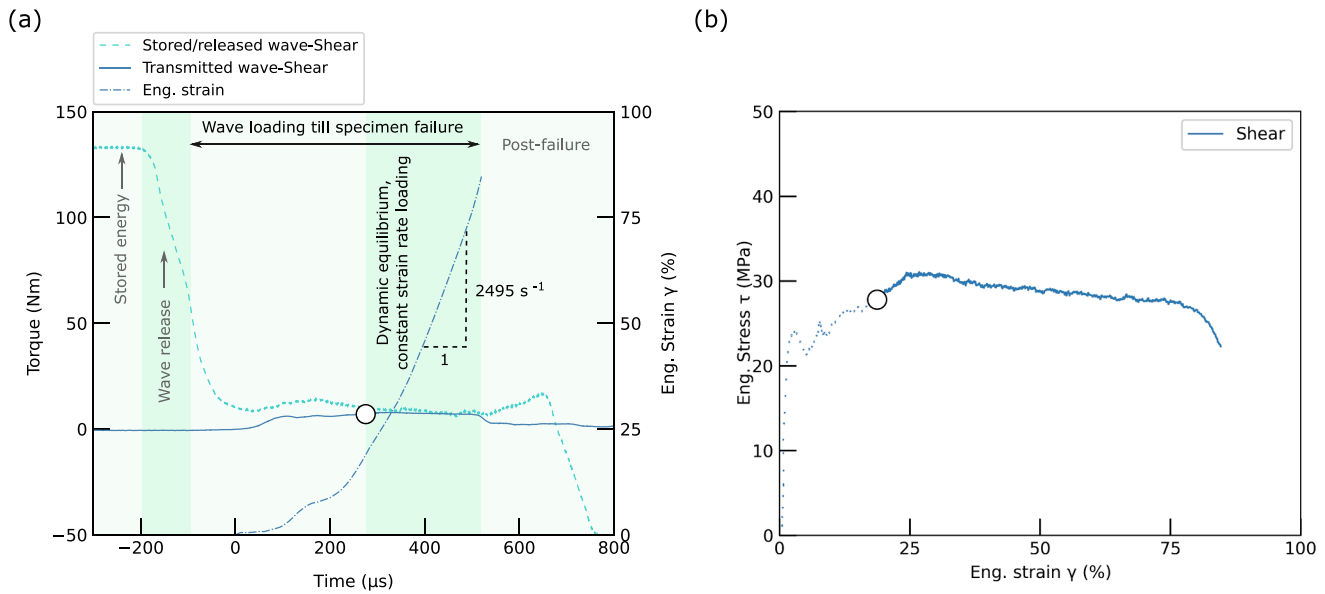


**Fig. 13.** High-rate monotonic torsional experiment of specimen #Z6: (a) time histories of the torques measured in the incident and transmitted bars, along with the history of the engineering shear strain from DIC analysis; (b) shear engineering stress–strain curve. Dynamic equilibrium was achieved from the point indicated by the white circle.

specimen appears more complicated as the ultimate stress exhibit strain rate insensitivity when the shear component prevails in the multiaxial stress state.

Note that the tensile stress in Fig. 16 refers to plane strain tension. It is therefore instructive to depict the failure stress loci in principal stress space ( $\sigma_1, \sigma_2$ ), as presented in Fig. 17.

This study focuses on the rate dependence of L-PBF processed PA12, which is a ductile thermoplastic polymer. Engineering ductile thermoplastic polymers typically exhibit a compressive strength that exceeds their tensile strength. As a result, these polymers are classified as asymmetric materials [52,53] due to variations in chain arrangement and deformation micro-mechanisms, which are influenced by the

hydrostatic stress level [54,55].

The original von Mises criterion can be modified to include pressure dependency by including a second term depending on the first invariant of the stress tensor  $I_1$  as follows:

$$J_2 = k^2 + \sum_{i=1}^n \alpha^i I_1^i \quad (9)$$

where,  $k$  and  $\alpha^i$  are constants that relate to the strength of the material and the effect of hydrostatic stress, respectively, and  $J_2$  is the second invariant of the deviatoric stress tensor.

Since the pressure dependency is associated with the difference between the compressive strength  $\sigma_c$  and tensile strength  $\sigma_t$ , a coefficient  $m$

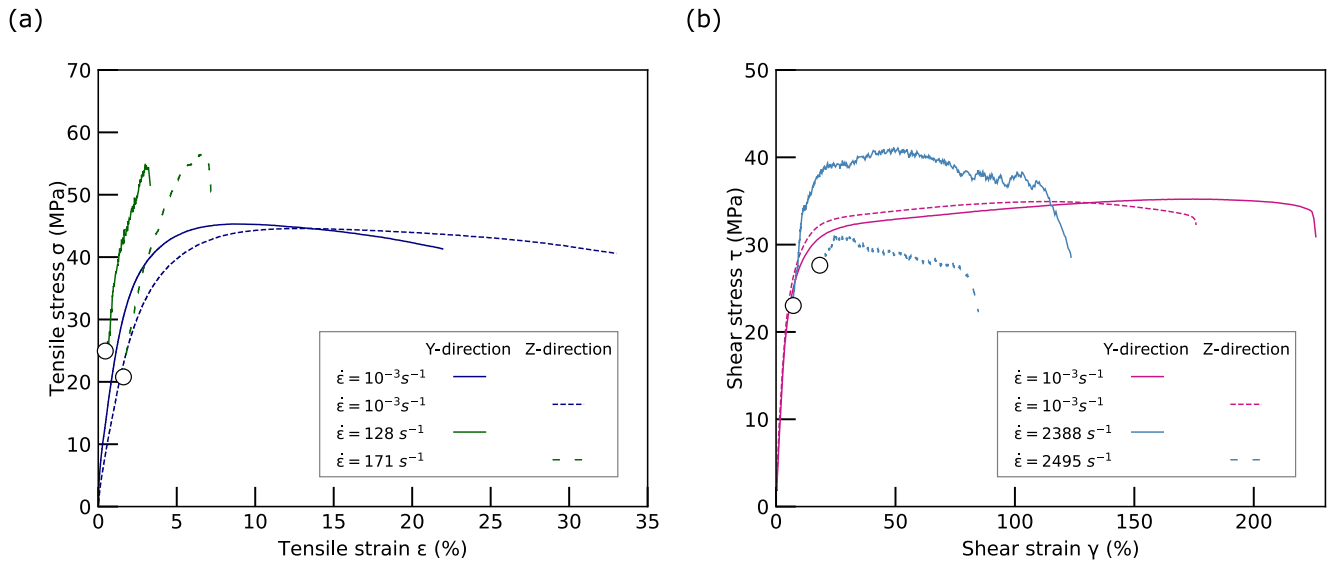


**Fig. 14.** Effect of strain rate on the stress–strain curves obtained from (a) monotonic tensile and (b) monotonic torsional loading. The high-rate stress–strain curves are shown from the point when dynamic equilibrium was achieved.

is introduced to characterise the level of the compression-tension asymmetry:

$$m = \frac{\sigma_c}{\sigma_t} \quad (10)$$

Previous studies successfully employed parabolically modified von Mises criteria to model the strength of a number of commercially produced polymers, including PA12 [56,57]. Similarly, here we consider  $n = 2$  in Eq. (9), namely considering the quadratic effect of hydrostatic stress, to obtain the parabolically modified von Mises model [56,58,59] as follows:

$$\sigma_{vM-P} = \frac{m-1}{2m} I_1 + \sqrt{\left(\frac{m-1}{2m} I_1\right)^2 + \frac{3J_2}{m}} \quad (11)$$

This model is fitted to describe the experimental measurements in the  $(\sigma_1, \sigma_2)$  plane via least square optimisation in Fig. 17. At quasi-static strain rate, the failure envelopes of Y- and Z-specimens nearly overlap with each other, with an asymmetry coefficient of 1.7 and 1.6, respectively. The available experimental data in the literature shows that the asymmetry coefficient of most thermoplastics varies from 1.0 to 1.8 [56]. The asymmetry coefficient is comparable to the results of L-PBF PA12 from Obst et al. [26], in which from the measured compressive strength and tensile strength the asymmetry coefficient of Y-samples and Z-samples are calculated in the range of 1.12–1.52 and 1.23–1.83, respectively. EOS powder PA2221 was employed in their studies.

It is noted that the assumption of volume constancy included in the above-mentioned criteria may not be rigorous at large strains, where the material may experience craze initiation and failure [60]. However, several studies employed the hypothesis of constant volume to successfully determine and model the mechanical behaviour of standard and additively manufactured PA12 [15,29,61]. This assumption was therefore deemed to be, in first approximation, appropriate to model the macroscopic behaviour of PA12 manufactured via laser powder bed fusion.

As the strain rate increases from low to high, the failure envelope of the Y-specimen expands concentrically outwards with the same asymmetry coefficient of 1.7. Whereas the failure envelope of the Z-specimen shifts towards to the origin and the asymmetry coefficient drastically reduces to 1.1. This indicates that the Y-specimen remains pronounced compression-tension asymmetry with the varying strain rate while the Z-specimen becomes more symmetric at high strain rates. The significant

change in the failure envelop of Z-specimens is the result of its strain rate insensitivity in shear. Since Y-specimens display comparable rate dependency in both tension and shear, the Z-specimens in comparison have dramatically lower ultimate shear strength, as well as shear-dominated combined ultimate strength. This new finding suggests, despite that the current L-PBF technology can produce PA12 parts with negligible anisotropy in strength in a quasi-static loading regime, caution is needed in dynamic loading conditions regarding the significant anisotropy resulted from the low inter-layer shear strength at a high strain rate.

As the main mechanism of failure is expected to be craze initiation and growth it is appropriate to interpolate the measured failure envelope in the  $(\sigma_1, \sigma_2)$  plane also using the Sternstein and Ongchin criterion [62–64], referred as the stress bias model. The criterion they proposed is in the form:

$$\sigma_b = |\sigma_1 - \sigma_2| = A(T) + \frac{B(T)}{\sigma_1 + \sigma_2 + \sigma_3} \quad (12)$$

where  $\sigma_b$  is referred as the ‘stress bias’ while  $A(T)$  and  $B(T)$  are material constants that remain fixed at a given temperature  $T$ .

The stress bias models approximated through the stress loci of Y- and Z-samples at quasi-static and high strain rates are compared to the parabolically modified von Mises models in Fig. 17. It is noted that the stress state of pure shear is an asymptotic line of the stress bias criterion and thus the ultimate strength in pure shear loading conditions is not considered. Consequently, the stress bias model cannot reflect the significant anisotropy in shear at high strain rates. Regardless of this, the stress bias model appears to well depict combined tension and torsion. However, a common criticism about this criterion is that it requires knowledge of the local stress state near the microscopic flaws, which is usually lacking. It is consequently difficult to apply the stress bias model. Questions are raised if the critical local stresses close to the craze are not directly and systematically related to the macroscopically applied stresses [64].

#### 4.4. Fracture morphology

The effects of the build direction and the strain rate are further assessed evaluating the fracture surfaces of the samples through post-mortem examination by means of Scanning Electron Microscopy (SEM) imaging. The SEM imaging was conducted in the tabletop

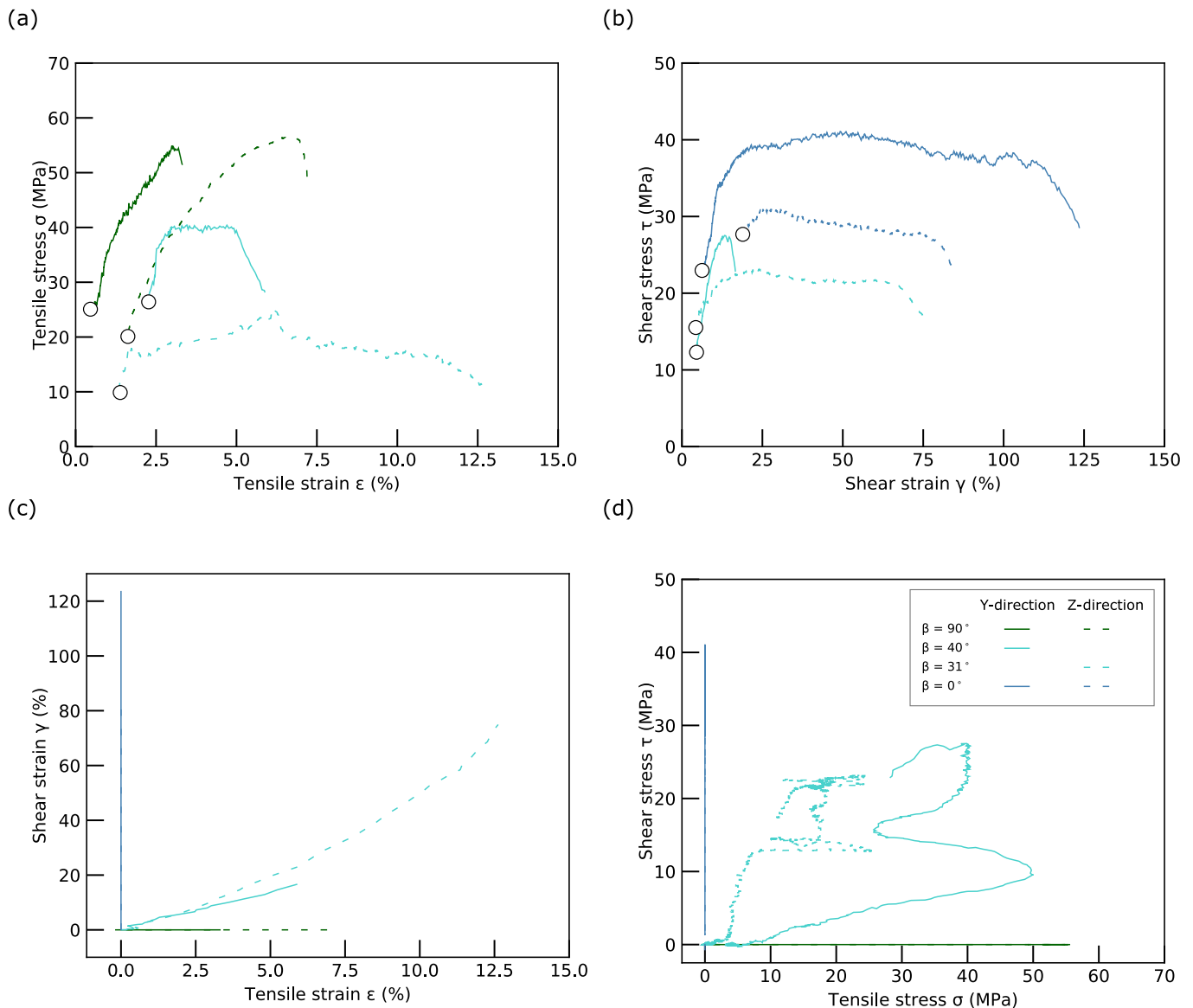


**Fig. 15.** Typical responses in different tensile-shear stress states at high rates of strain: engineering stress–strain curves in (a) tension and (b) shear, along with the trajectories of (c) shear strain versus tensile strain and (d) shear stress versus tensile stress. The stress–strain curves are shown from the point when dynamic equilibrium was achieved.

microscope TM3030Plus (Hitachi, Japan) using the BSE detector and 15 kV accelerating voltage.

The fracture surfaces of Y- and Z- specimens after tensile tests at varied strain rates are compared in Fig. 18. Pores and voids are revealed. Unmolten particles could be readily observed on the surface of the thin-walled tube specimen, coalesced and clustered with neighbouring particles. The size of the unmolten particles varies however is apparently smaller than the diameter of the raw PA2200 powder 58  $\mu\text{m}$  (Table 1). Within the semi-crystalline microstructure of PA12, the crystallised spherulite chains could get molten during laser melting, whereas the aggregated polymer molecules in the core region of the spherulites can remain unmolten [65]. As a result of rapid crystallisation and hence shrinkage and particle detachment during L-PBF process, porosities cannot be avoided but always exist in L-PBF parts if using single laser scanning. Meanwhile, clustered unmolten particles on the surface of the parts are another indicator of the partial melting of the powders.

In the case of quasi-static tensile loading (Fig. 18a–b), the unmolten particles or particle clusters are torn from the merged matrix and eventually pulled out, resulting in deep and large dimples featuring torn

filaments that are stretched in the loading direction. The torn dimples and stretched filaments are also observed in other research of the tensile fracture of PA12 [13,66] and indicates a substantially high level of polymer ductility. The more elongated filament out of the fracture surface of the Z-specimen shows that the latter is more ductile than the Y-specimen, in consistency with the strain measurements (Fig. 7a).

Cleavage facet is a distinctive feature of the fracture surface retrieved from high rate tensile loading tests (Fig. 18c–d). In contrast to the high ductility of PA12 at quasi-static loading rate, the fracture appears more brittle at high strain rates, shown as smaller and fewer pores without torn filaments. Secondary cracks and flat craze flakes could be readily noticed on the cleavage facets. The flake structure is also observed in research into the dynamic fracture of PA12 pipe specimens, resulted from adiabatic decohesion during rapid crack propagation [67]. As this flake structure appears more prominent on the fractography of the Z-specimen than that of the Y-specimen, the layered structure of the Z-specimen (Fig. 5b) might be another underlying mechanism that arises multi-layer fracture and the subsequent craze flakes. The observation agrees with the significantly smaller strain measurements at high-rate

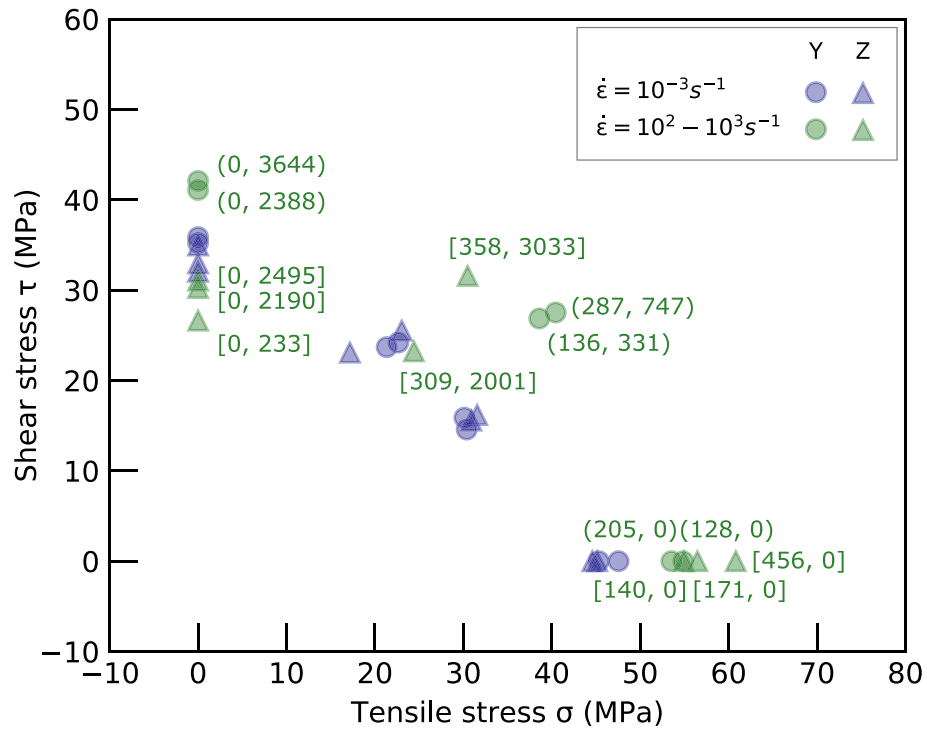


Fig. 16. Ultimate stress loci in shear versus tensile stress space.

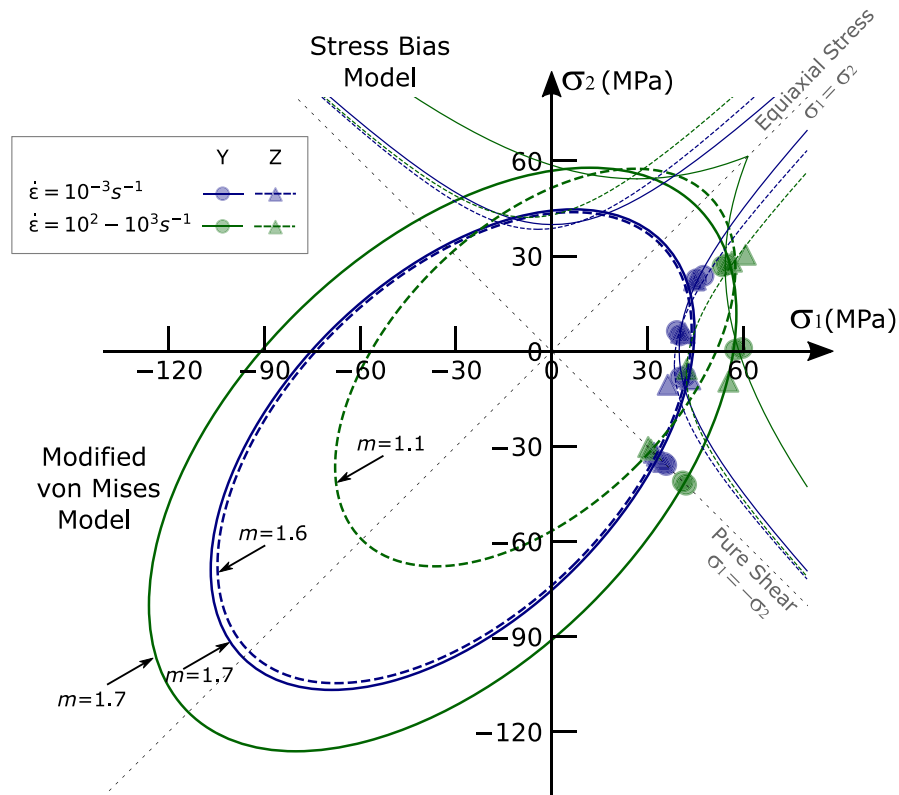
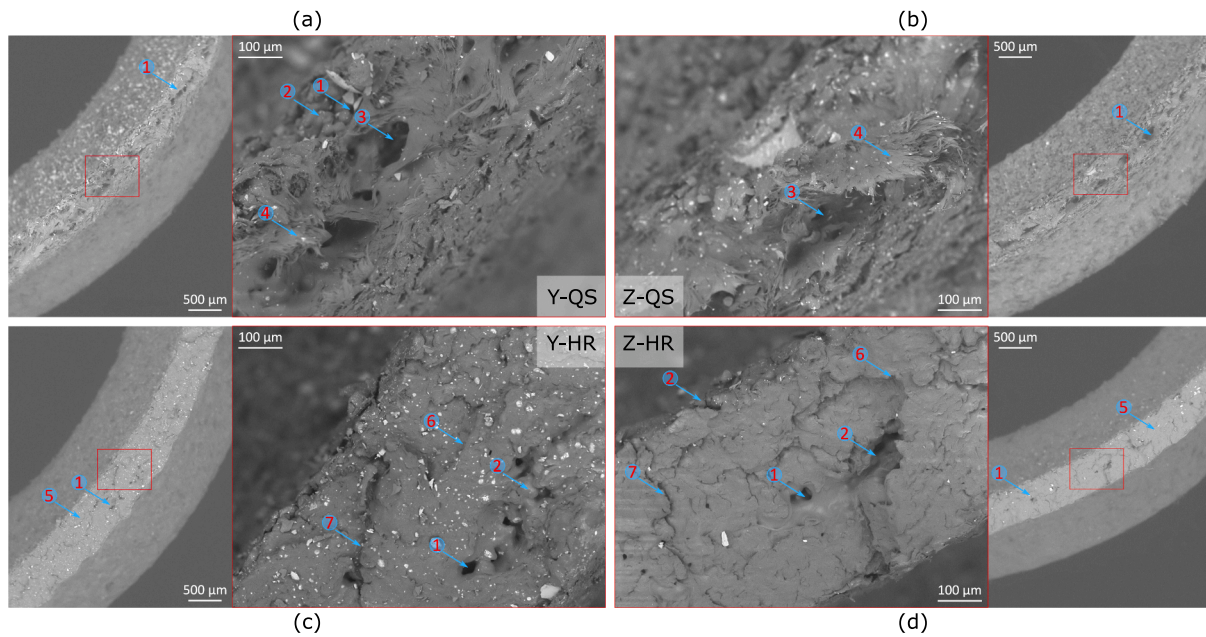
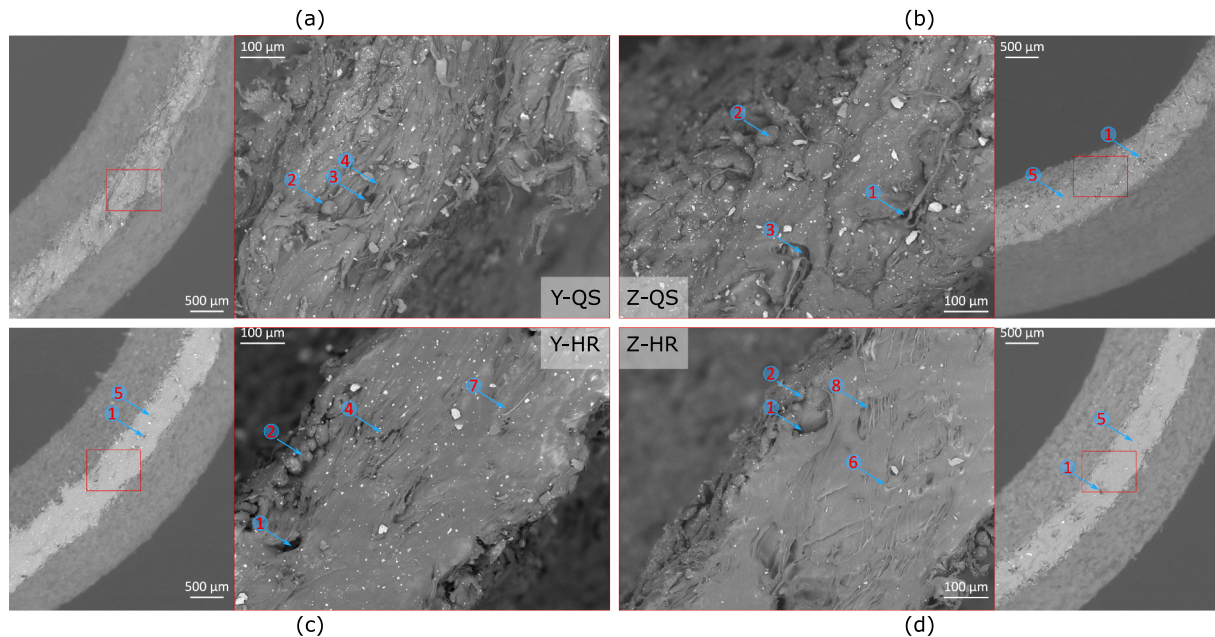


Fig. 17. Ultimate stress loci in principal stress space and prediction by the parabolically modified von Mises model and the stress bias model (Sternstein and Ongchin criterion).





**Fig. 18.** Scanning electron micrographs of the fracture surface of PA12 retrieved from tensile tests: (a) Y-specimen #Y2 and (b) Z-specimen #Z8 at quasi-static loading; (c) Y-specimen #Y6 and (d) Z-specimen #Z12 at high-rate loading. Annotations: 1-Pores and voids; 2-Unmolten particles; 3-Torn dimples; 4-Stretched filaments out of the fracture surface; 5-Cleavage facets; 6-Craze flakes; 7-Secondary cracks.



**Fig. 19.** Scanning electron micrographs of the fracture surface of PA12 retrieved from torsional tests: (a) Y-specimen #Y12 and (b) Z-specimen #Z14 at quasi-static loading; (c) Y-specimen #Y10 and (d) Z-specimen #Z6 at high-rate loading. Annotations: 1-Pores and voids; 2-Unmolten particles; 3-Torn dimples; 4-Stretched filaments along the shearing direction on the fracture surface; 5-Cleavage facets; 6-V-shaped fibrils oriented in the shearing direction; 7-Parabolic fibrils oriented in the shearing direction; 8-Parallel fibrils at the edge of craze flakes.

loading than those at a low strain rate.

The fractography of Y- and Z- specimens after torsional tests at varied strain rates is summarised in Fig. 19. Commonly observed are pores and unmolten particles as the intrinsic features from L-PBF processing. In the case of quasi-static loading, fewer pores are exposed on the shear fracture surface compared to tensile fractography, plausibly because filaments are torn and stretched in the shearing direction, leaving possible voids or dimples covered by the elongated filaments. This indication of significantly high ductility is consistent with the experimental

measurements of large shear deformation (Fig. 7b). Meanwhile, cleavage facets could be observed on the fractography of the Z-specimen (Fig. 19b). This might be attributed to the inter-layer shearing that reduces the filaments being torn and stretched out of the layer as observed from the Y-specimen (Fig. 19a).

Cleavage facet with fibrillar structures highlights the high-rate torsional fractography (Fig. 19c-d). At high-rate loading, the crack initiates and then propagates at a high speed, during which large amounts of energy are ultimately converted into heat. Due to the low thermal

conductivity of polyamides, the rapid crack propagation is accompanied with adiabatic heating effect [67]. As the strain rates of the torsional tests is one order higher than those of the tensile tests conducted in this study (see Table 3 or Fig. 16), the adiabatic heating effect is more profound within the plastic zone at the crack front of mode-II fracture. More polymer chains are fused and disentangled into fibrillar structures, which eventually separate, promoted by adiabatic decohesion. The separated fibrils remain on the fracture surface featuring various patterns, such as parabolic on the Y-specimen and V-shaped on the Z-specimen, oriented in the direction of shear. The fibrillar structure at the edge of flakes appears to be strong evidence of adiabatic heating and rapid decohesion [67].

Furthermore, the fracture surface of the Z-HR specimen is characterised by higher smoothness covered by a larger number of finer fused fibrils than that of the Y-HR specimen. This indicates more heat generated at the high-rate event. The rapid increase of the local temperature could contribute to the deterioration of the mechanical properties [29], resulting in the dynamic shear strength of the Z-HR specimens to be inferior to that of the Y-HR specimens, as measured in Section 4.2.

High-rate loading causes rapid crack propagation, during which adiabatic heating and decohesion take place due to the coupling of the thermal and mechanical loading conditions. Yet the intrinsic reason for the higher level of heat accumulation and adiabatic decohesion of Z-specimens remains unclear. It might be attributed to the change of the inter-layer thermal conductivity of the L-PBF specimen from the manufacturing process. The influence of process parameters including the scanning hatch distance, layer thickness, and especially energy density, has been addressed in the literature. These parameters can change crystallisation and residual porosity, which eventually affects the thermal conductivity [5,10–12]. It has also been well studied that, porosity is unquestionably the key factor influencing the mechanical behaviour of AM polymer parts [7], since a variety of mechanical responses can be explained by different porosity levels, as well as the shape, diameter, volume and relative distributions of the pores and voids [16,68]. In this study, we have measured identical tensile strength of Y- and Z- samples at both low and high strain rates. Comparable shear strength of Y- and Z- samples was also obtained at a low strain rate. Until this point, we could conclude that the porosity resulted from the L-PBF process appear to possess similar characteristics in both Y- and Z- samples, and that the porosity-related anisotropy is negligible. However, later we measured a significant discrepancy between the dynamic shear strength of Y- and Z- samples. This might suggest an unknown influence the porosity has on the inter-layer shear strength, due to changes in the inter-layer thermal conductivity and therefore in the high-rate shear behaviour associated with adiabatic heating and rapid decohesion. Future work that links the forming behaviours of the L-PBF polymer parts (e.g., porosity and thermal conductivity) and the mechanical behaviours is needed to understand the unexpected anisotropy in shear at high strain rates.

Additionally, to improve the physical and mechanical properties of L-PBF parts, modifications have been developed into the L-PBF manufacturing techniques to alter the intrinsic features including crystallisation, residual porosity, and thermal conductivity etc. For instance, addition of micron-sized inorganic fillers (e.g., aluminium powders) or nano-sized fillers (e.g., carbon nanoparticles/fibres) can change the melting and crystallisation behaviour of the polymer feedstock and thus improve pore formation and mechanical properties [6,69]; a warm isostatic press process can increase crystallisation meanwhile reducing porosities and consequently improve the thermal conductivity of L-PBF processed PA12 parts [19]. Future work will include investigations on the capability of these emerging modifications on the L-PBF process to enhance the dynamic strength, especially the inter-layer shear strength, from the perspectives of improving the porosity and thermal conductivity.

## 5. Conclusions

The tensile-shear behaviour of additively manufactured PA12 via laser powder bed fusion is experimentally investigated meanwhile considering the effects of the build orientation and the strain rate ranging from  $10^{-3}$  to  $10^3 \text{ s}^{-1}$ . A combined tension–torsion Hopkinson bar apparatus was employed to implement the multiaxial loading experiments at high strain rates. A variety of stress states were achieved from the combined tension–torsion loading experiments involving pure shear, plane strain tension, uniaxial tension, and combined tension–shear with various ratios between the tensile and shear components. The failure loci are constructed in the principal stress space. The main conclusions are as follows:

- 1) In the regime of quasi-static loading, the build direction barely shows influence on either the ultimate tensile strength or the ultimate shear strength. The maximum stress envelopes of the Y- and Z- specimens are nearly overlapped, characterised with pronounced compression–tension asymmetry ranging from 1.6 to 1.7.
- 2) As the strain rate increases, apparent positive rate dependence is shown on the ultimate tensile strength of both specimens but with dramatically reduced elongation at break. The ultimate shear strength of the Y-specimens exhibits comparable rate dependence as its tensile counterpart, whereas the shear strength of the Z-specimens appears insensitive to the strain rate. Consequently, the ultimate stress envelope of the Y-specimen maintains the compression–tension asymmetry around 1.7, while the Z-specimen exhibits considerably low asymmetry coefficient of 1.1.
- 3) The rate-dependent characteristics of post-mortem fractography agree with the experimental measurements, both demonstrating the ductility of the material in a quasi-static loading regime whereas the increasing brittleness at high strain rates. The craze flakes on the fracture surface suggest brittle fracture in high-rate tension, while fibrils indicate adiabatic heating and rapid decohesion in high-rate shear loading.

From this investigation, the direct measurements of the stress–strain curves obtained from multiaxial loading tests at various strain rates can contribute to verifying material models of PA12 manufactured by L-PBF that are usually calibrated from simple loading scenarios.

Attention shall be raised in dynamic applications as anisotropy can be significant due to the low inter-layer shear strength at high strain rates, despite that the current established L-PBF process can fabricate PA12 parts with negligible anisotropy in strength in the quasi-static loading regime.

Future work will focus on the influence of the intrinsic features of L-PBF parts resulted from the manufacturing process on their macroscopic multiaxial behaviours at a high strain rate. The aim is to establish the relationship between the mechanical behaviours and the forming behaviours regarding the crystallisation, porosity, and thermal conductivity etc. This will contribute to identifying the underlying mechanism of the mechanical behaviours, especially the unexpected significant anisotropy at high strain rates, and eventually provide a better guide on improving the L-PBF techniques and developing stronger L-PBF parts in end-use applications.

## Declaration of Competing Interest

The authors declare that they have no known competing financial interests or personal relationships that could have appeared to influence the work reported in this paper.

## Data availability

The raw/processed data required to reproduce these findings cannot be shared at this time as the data also forms part of an ongoing study.

## Acknowledgement

The authors would like to thank Rolls-Royce plc. and the EPSRC for the support under the Prosperity Partnership Grant \Cornerstone: Mechanical Engineering Science to Enable Aero Propulsion Futures, Grant Ref: EP/R004951/1. Additionally the authors would like to thank to Dr Arnaud Regazzi from IMT Mines Alès for providing the AM samples used in this study.

## References

- [1] Y. Wang, Z. Xu, D. Wu, J. Bai, Current status and prospects of polymer powder 3D printing technologies, *Materials* (Basel) (2020) 13, <https://doi.org/10.3390/ma13102406>.
- [2] M. Picard, A.K. Mohanty, M. Misra, Recent advances in additive manufacturing of engineering thermoplastics: challenges and opportunities, *RSC Adv.* 10 (59) (2020) 36058–36089.
- [3] ISO/ASTM International. Additive Manufacturing - General Principles Terminology (ASTM52900). Rapid Manuf Assoc 2013;2021:10–2.
- [4] B. Van Hooreweder, D. Moens, R. Boonen, J.P. Kruth, P. Sas, On the difference in material structure and fatigue properties of nylon specimens produced by injection molding and selective laser sintering, *Polym. Test* 32 (2013) 972–981, <https://doi.org/10.1016/j.polymertesting.2013.04.014>.
- [5] M. Grünewald, K. Popp, J. Rudloff, M. Lang, A. Sommereyns, M. Schmidt, S. Mohseni-Mofidi, C. Bierwisch, Experimental, numerical and analytical investigation of the polyamide 12 powder bed fusion with the aim of building dimensionless characteristic numbers, *Mater. Des.* 201 (2021) 109470.
- [6] R.D. Goodridge, C.J. Tuck, R.J.M. Hague, Laser sintering of polyamides and other polymers, *Prog. Mater. Sci.* 57 (2012) 229–267, <https://doi.org/10.1016/j.pmatsci.2011.04.001>.
- [7] R. Brighenti, M.P. Cosma, L. Marsavina, A. Spagnoli, M. Terzano, Laser-based additively manufactured polymers: a review on processes and mechanical models, *J. Mater. Sci.* 56 (2021) 961–998, <https://doi.org/10.1007/s10853-020-05254-6>.
- [8] J.R.C. Dizon, A.H. Espora, Q. Chen, R.C. Advincula, Mechanical characterization of 3D-printed polymers, *Addit. Manuf.* 20 (2018) 44–67, <https://doi.org/10.1016/j.addma.2017.12.002>.
- [9] A. Nazir, O. Gokcekaya, K. Md Masum Billah, O. Ertugrul, J. Jiang, J. Sun, S. Hussain, Multi-material additive manufacturing: A systematic review of design, properties, applications, challenges, and 3D Printing of materials and cellular metamaterials, *Mater. Des.* 226 (2023) 111661.
- [10] D.I. Stoia, L. Marsavina, E. Linul, Correlations between process parameters and outcome properties of laser-sintered polyamide, *Polymers* (Basel) (2019) 11, <https://doi.org/10.3390/polym11111850>.
- [11] Z. Zhu, C. Majewski, Understanding pore formation and the effect on mechanical properties of High Speed Sintered polyamide-12 parts: A focus on energy input, *Mater. Des.* (2020) 194, <https://doi.org/10.1016/j.matdes.2020.108937>.
- [12] B. Caulfield, P.E. McHugh, S. Lohfeld, Dependence of mechanical properties of polyamide components on build parameters in the SLS process, *J. Mater. Process. Technol.* 182 (2007) 477–488, <https://doi.org/10.1016/j.jmatprotec.2006.09.007>.
- [13] B. Yao, Z. Li, F. Zhu, Effect of powder recycling on anisotropic tensile properties of selective laser sintered PA2200 polyamide, *Eur. Polym. J.* 141 (2020), 110093, <https://doi.org/10.1016/j.eurpolymj.2020.110093>.
- [14] Zarringhalam H, Hopkinson N, Kamperman NF, Vlieger JJ De. Effects of processing on microstructure and properties of SLS Nylon 12 2006;436:172–80. <https://doi.org/10.1016/j.msea.2006.07.084>.
- [15] S. Rosso, R. Meneghello, L. Biasetto, L. Grigolato, G. Concheri, G. Savio, In-depth comparison of polyamide 12 parts manufactured by Multi Jet Fusion and Selective Laser Sintering, *Addit. Manuf.* 36 (2020), 101713, <https://doi.org/10.1016/j.addma.2020.101713>.
- [16] F. Calignano, F. Giuffrida, M. Galati, Effect of the build orientation on the mechanical performance of polymeric parts produced by multi jet fusion and selective laser sintering, *J. Manuf. Process.* 65 (2021) 271–282, <https://doi.org/10.1016/j.jmapro.2021.03.018>.
- [17] J. Schneider, S. Kumar, Multiscale characterization and constitutive parameters identification of polyamide (PA12) processed via selective laser sintering, *Polym. Test.* 86 (2020), 106357, <https://doi.org/10.1016/j.polymertesting.2020.106357>.
- [18] A.J. Cano, A. Salazar, J. Rodríguez, Effect of temperature on the fracture behavior of polyamide 12 and glass-filled polyamide 12 processed by selective laser sintering, *Eng. Fract. Mech.* 203 (2018) 66–80, <https://doi.org/10.1016/j.engfracmech.2018.07.035>.
- [19] S.J. Park, J.W. Choi, S.J. Park, Y. Son, I.H. Ahn, Improving properties of a part fabricated by polymer-based powder bed fusion using a warm isostatic press (WIP) process, *Mater. Des.* 224 (2022), 111417, <https://doi.org/10.1016/j.matdes.2022.111417>.
- [20] F. Mehdipour, U. Gebhardt, M. Kästner, Anisotropic and rate-dependent mechanical properties of 3D printed polyamide 12 - A comparison between selective laser sintering and multi jet fusion, *Results Mater* (2021) 11, <https://doi.org/10.1016/j.rinma.2021.100213>.
- [21] M. Crespo, T. Gómez-del Río, J. Rodríguez, Failure of polyamide 12 notched samples manufactured by selective laser sintering, *J. Strain Anal. Eng. Des.* 54 (2019) 192–198, <https://doi.org/10.1177/0309324719847817>.
- [22] U. Ajoku, N. Saleh, N. Hopkinson, R. Hague, P. Erasenthiran, Investigating mechanical anisotropy and end-of-vector effect in laser-sintered nylon parts, *Proc. Inst. Mech. Eng. Part B J. Eng. Manuf.* 220 (2006) 1077–1086, <https://doi.org/10.1243/0954045JEM537>.
- [23] S. Dupin, O. Lame, C. Barrès, J.Y. Charneau, Microstructural origin of physical and mechanical properties of polyamide 12 processed by laser sintering, *Eur. Polym. J.* 48 (2012) 1611–1621, <https://doi.org/10.1016/j.eurpolymj.2012.06.007>.
- [24] A. Salazar, A. Rico, J. Rodríguez, J. Segurado Escudero, R. Seltzer, M. De La Escalera, F. Cutillas, Fatigue crack growth of SLS polyamide 12: Effect of reinforcement and temperature, *Compos. B Eng.* 59 (2014) 285–292, <https://doi.org/10.1016/j.compositesb.2013.12.017>.
- [25] G.A. Mazzei Capote, A. Redmann, T.A. Osswald, Validating a failure surface developed for abs fused filament fabrication parts through complex loading experiments, *J. Compos. Sci.* (2019); 3, <https://doi.org/10.3390/jcs3020049>.
- [26] P. Obst, M. Launhardt, D. Drummer, P.V. Osswald, T.A. Osswald, Failure criterion for PA12 SLS additive manufactured parts, *Addit. Manuf.* 21 (2018) 619–627.
- [27] T. Gómez-del Río, M. Crespo, R. López, J. Rodríguez, Effect of strain rate on tensile fracture behavior of notched polyamide 12 processed by selective laser sintering, *Theor. Appl. Fract. Mech.* 121 (2022), 103434, <https://doi.org/10.1016/j.tafmec.2022.103434>.
- [28] Narsimlu K. A market analysis on the impact of additive layer manufacturing technologies on aerospace and defense supply chain Chandrashekhavar Yavarna, A Market Analysis On The Impact of Additive Layer Manufacturing Technologies On Aerospace and Defense Supply Chain. *Artic ID IJM\_08\_02\_019 Int J Manag n.d.*;8: 171–87.
- [29] D.A. Şerban, G. Weber, L. Marşavina, V.V. Silberschmidt, W. Hufenbach, Tensile properties of semi-crystalline thermoplastic polymers: Effects of temperature and strain rates, *Polym. Test.* 32 (2013) 413–425, <https://doi.org/10.1016/j.polymertesting.2012.12.002>.
- [30] A.S. Argon, *The Physics of Deformation and Fracture of Polymers* | Materials Science ], Cambridge University Press, 2013.
- [31] J.E.T. Cook, R.D. Goodridge, C.R. Siviour, E. Cadoni, Strain rate dependency of laser sintered polyamide 12, *EPJ Web Conf.* 94 (2015) 02019.
- [32] M. Crespo, M.T. Gómez-del Río, J. Rodríguez, Failure of SLS polyamide 12 notched samples at high loading rates, *Theor. Appl. Fract. Mech.* 92 (2017) 233–239, <https://doi.org/10.1016/j.tafmec.2017.08.008>.
- [33] M.J. Kendall, C.R. Siviour, Rate dependence of poly(vinyl chloride), the effects of plasticizer and time-temperature superposition, *Proc. R. Soc. A* 470 (2167) (2014) 20140012.
- [34] C.R. Siviour, J.L. Jordan, High strain rate mechanics of polymers: a review, *J. Dyn. Behav. Mater.* 2 (1) (2016) 15–32.
- [35] A.R. Trivedi, P. Song, C.R. Siviour, Experimentally simulating adiabatic behaviour: Capturing the high strain rate compressive response of polymers using low strain rate experiments with programmed temperature profiles, *Polym. Test.* 116 (2022) 107773.
- [36] Furmanskij J, Cady CM, Brown EN. Time-temperature equivalence and adiabatic heating at large strains in high density polyethylene and ultrahigh molecular weight polyethylene 2012. <https://doi.org/10.1016/j.polymer.2012.11.010>.
- [37] V. Gonda, J. Den Toonder, J. Beijer, G.Q. Zhang, L.J. Ernst, Finite thickness influence on spherical and conical indentation on viscoelastic thin polymer film, *J. Electron. Packag.* 127 (2005) 33–37, <https://doi.org/10.1115/1.1846065>.
- [38] B. Pan, Z. Lu, H. Xie, Mean intensity gradient: An effective global parameter for quality assessment of the speckle patterns used in digital image correlation, *Opt. Lasers Eng.* 48 (2010) 469–477, <https://doi.org/10.1016/j.optlaseng.2009.08.010>.
- [39] G. Quino, Y. Chen, K.R. Ramakrishnan, F. Martínez-Hergueta, G. Zumpano, A. Pellegrino, N. Petrinic, Speckle patterns for DIC in challenging scenarios: rapid application and impact endurance, *Meas. Sci. Technol.* 32 (1) (2021) 015203.
- [40] Y. Xu, J. Zhou, L. Farbaniec, A. Pellegrino, Optimal design, development and experimental analysis of a tension-torsion Hopkinson bar for the understanding of complex impact loading scenarios, *Exp. Mech.* 2023 (2023) 1–17, <https://doi.org/10.1007/s11340-023-00942-1>.
- [41] Xu Y, Farbaniec L, Siviour C, Eakins D, Pellegrino A. The Development of Split Hopkinson Tension-Torsion Bar for the Understanding of Complex Stress States at High Rate, 2021, p. 89–93. [https://doi.org/10.1007/978-3-030-59947-8\\_16](https://doi.org/10.1007/978-3-030-59947-8_16).
- [42] Y. Xu, M.A. Lopez, J. Zhou, L. Farbaniec, S. Patsias, D. Macdougall, J. Reed, N. Petrinic, D. Eakins, C. Siviour, A. Pellegrino, Experimental analysis of the multiaxial failure stress locus of commercially pure titanium at low and high rates of strain, *Int. J. Impact Eng* 170 (2022) 104341.
- [43] J. Zhou, Y. Xu, M.A. Lopez, L. Farbaniec, S. Patsias, D. Macdougall, J. Reed, N. Petrinic, D. Eakins, C. Siviour, A. Pellegrino, The mechanical response of commercially pure copper under multiaxial loading at low and high strain rates, *Int. J. Mech. Sci.* 224 (2022) 107340.
- [44] H. Kolsky, Stress waves in solids, *J. Sound Vib.* 1 (1964) 88–110, [https://doi.org/10.1016/0022-460X\(64\)90008-2](https://doi.org/10.1016/0022-460X(64)90008-2).
- [45] C. Cai, W.S. Tey, J. Chen, W. Zhu, X. Liu, T. Liu, L. Zhao, K. Zhou, Comparative study on 3D printing of polyamide 12 by selective laser sintering and multi jet fusion, *J. Mater. Process. Technol.* 288 (2021) 116882.
- [46] ASTM. D638-14: Standard Test Method for Tensile Properties of Plastics. ASTM Int. West Conshohocken, PA, 2014.
- [47] ISO. ISO 527-1: Plastics — Determination of tensile properties — Part 1: General principles. ISO/TC 61/SC 2 Mech. Behav., 2012.
- [48] ISO. ISO 527-2: Plastics — Determination of tensile properties — Part 2: Test conditions for moulding and extrusion plastics. ISO/TC 61/SC 2 Mech. Behav., 2012.



- [49] Z. Xu, Y. Wang, D. Wu, K.P. Ananth, J. Bai, The process and performance comparison of polyamide 12 manufactured by multi jet fusion and selective laser sintering, *J. Manuf. Process.* 47 (2019) 419–426, <https://doi.org/10.1016/j.jmapro.2019.07.014>.
- [50] Bajerski P, Pecherski RB, Chudy D, Jarecki L. Crystallization Kinetics of Polyamide 2200 in the Modelling of Additive Manufacturing Processes by FE Analyses. *Eng Trans* 2019;67:301–309. <https://doi.org/10.24423/ENGTRANS.1013.20190729>.
- [51] L. Benedetti, B. Brulé, N. Decraemer, K.E. Evans, O. Ghita, Shrinkage behaviour of semi-crystalline polymers in laser sintering: PEKK and PA12, *Mater. Des.* (2019) 181, <https://doi.org/10.1016/j.MATDES.2019.107906>.
- [52] J. Rösler, H. Harders, M. Bäker, Mechanical behaviour of engineering materials: Metals, ceramics, polymers, and composites, *Mech. Behav. Eng. Mater. Met. Ceram. Polym. Compos.* (2007) 1–534, <https://doi.org/10.1007/978-3-540-73448-2/COVER>.
- [53] Bower D. An Introduction to Polymer Physics. New York: Cambridge University Press; 2002. <https://doi.org/10.1017/CBO9780511801280.002>.
- [54] Ward IM, Sweeney J. Mechanical Properties of Solid Polymers: Third Edition. *Mech Prop Solid Polym Third Ed* 2012. <https://doi.org/10.1002/9781119967125>.
- [55] R. Raghava, R.M. Caddell, G.S.Y. Yeh, The macroscopic yield behaviour of polymers, *J. Mater. Sci.* 8 (1973) 225–232, <https://doi.org/10.1007/BF00550671/METRICS>.
- [56] G.H.B. Donato, M. Bianchi, Pressure dependent yield criteria applied for improving design practices and integrity assessments against yielding of engineering polymers, *J. Mater. Res. Technol.* 1 (2012) 2–7, [https://doi.org/10.1016/S2238-7854\(12\)70002-9](https://doi.org/10.1016/S2238-7854(12)70002-9).
- [57] E. Ghorbel, A viscoplastic constitutive model for polymeric materials, *Int. J. Plast.* 24 (2008) 2032–2058, <https://doi.org/10.1016/j.ijplas.2008.01.003>.
- [58] E. Miller, M. Dekker, Introduction to Plastics and Composites: Mechanical Properties and Engineering Applications. New York, USA 1996;30:448.
- [59] G.W. Ehrenstein, G. Erhard, *Designing with Plastics: A Report on the State of the Art*, Ger Carl Hanser Verlag Rep, Munich, 1994 <https://www.abebooks.co.uk/Designing-Plastics-Report-State-Art-Ehrenstein/13113190123/bd> (accessed October 17, 2022).
- [60] M. Martínez, A.J. Cano, A. Salazar, J. Rodríguez, On the failure assessment diagram methodology in polyamide 12, *Eng. Fract. Mech.* (2022) 269, <https://doi.org/10.1016/j.engfracmech.2022.108558>.
- [61] H. Rahman, E. Yarali, A. Zolfagharian, A. Serjouei, M. Bodaghi, Energy absorption and mechanical performance of functionally graded soft–hard lattice structures, *Materials (Basel)* (2021) 14, <https://doi.org/10.3390/ma14061366>.
- [62] S.S. Sternstein, L. Ongchin, Yield criteria for plastic deformation of glassy high polymers in general stress fields. *Polymer preprints, Polym. Prepr.* 10 (1969) 1117–1124.
- [63] R.J. Oxborough, P.B. Bowden, A general critical-strain criterion for crazing in amorphous glassy polymers, *Phil. Mag.* 28 (1973) 547–559, <https://doi.org/10.1080/14786437308221002>.
- [64] C.B. Bucknall, New criterion for craze initiation, *Polymer (Guildf)* 48 (4) (2007) 1030–1041.
- [65] S. Dadbakhsh, L. Verbelen, O. Verkinderen, D. Strobbe, P. Van Puyvelde, J. P. Kruth, Effect of PA12 powder reuse on coalescence behaviour and microstructure of SLS parts, *Eur. Polym. J.* 92 (2017) 250–262, <https://doi.org/10.1016/J.EURPOLYMJ.2017.05.014>.
- [66] S. Ghaemi Khiavi, B. Mohammad Sadeghi, M. Divandari, Effect of topology on strength and energy absorption of PA12 non-auxetic strut-based lattice structures, *J. Mater. Res. Technol.* 21 (2022) 1595–1613.
- [67] M. Messiha, A. Frank, J. Heimink, F. Arbeiter, G. Pinter, Mechanisms of rapid fracture in PA12 grades, *Theor. Appl. Fract. Mech.* (2022) 117, <https://doi.org/10.1016/J.TAFMEC.2021.103145>.
- [68] K.P.M. Lee, C. Pandelidi, M. Kajtar, Build orientation effects on mechanical properties and porosity of polyamide-11 fabricated via multi jet fusion, *Addit. Manuf.* 36 (2020), 101533, <https://doi.org/10.1016/j.addma.2020.101533>.
- [69] G. Flodberg, H. Pettersson, L. Yang, Pore analysis and mechanical performance of selective laser sintered objects, *Addit. Manuf.* 24 (2018) 307–315, <https://doi.org/10.1016/J.ADDMA.2018.10.001>.